Computational Particle Mechanics manuscript No.
(will be inserted by the editor)

Material interface modeling by the enriched RKPM with stabilized nodal integration

Huy Anh Nguyen [1] · **Satoyuki Tanaka** [1] · **Tinh Quoc Bui**[2,3]

Received: date / Accepted: date

Abstract In this paper, an enriched reproducing kernel particle method combined with stabilized conforming nodal integration (SCNI) is proposed to tackle material interface problems. Regarding the domain integration, the use of SCNI offers an effective NI technique and eliminates the zero-energy modes which occurs to direct NI. To model material interfaces, the method enriches the approximation by adding special functions constructed based on the level set function to represent weak discontinuities. Numerical examples with simple and complicated geometries of interface problems in two-dimensional linear elasticity are presented to test the performance of the proposed method, and results show that it considerably reduces strain oscillations and yields optimal convergence rates.

Keywords Meshfree method, Nodal integration, Material interface, Enrichment, Assumed strain

1 Introduction

Meshfree methods (MFs) have been extensively developed over the past two decades since the seminal works of Belytschko and coworkers [1] on the element-free Galerkin (EFG) method, and then a great number of other MFs were proposed such as reproducing kernel particle method (RKPM) [2], h-p cloud method [3], meshless local Petrov-Galerkin method [4], method of finite spheres [5], local maximum-entropy method [6], among others.

The common feature of MFs is that their approximation is constructed based on only scattered nodes in the domain, so it bypasses the need for obtaining high-quality mesh. Consequently, the drawbacks of mesh-based methods such as finite element method (FEM) can be circumvented, and there have existed a large body of literature in MFs about large deformation [7,8], fracture [9–12], plates and shells [13–15] and others. Furthermore, the order of continuity and completeness of MF approximation can be controlled independently from one another, thus one can be varied while the other is fixed. As a result, it offers a huge advantage of solving PDEs involving high-order derivatives. Furthermore, there are additional benefits provided by MFs such as easy implementation of h- and p- refinement and straightforward enrichment of approximation by a priori feature of the solution under consideration.

Possessing all of these attractive properties, MFs show their potential for the effective solutions to PDEs. However, similar to other numerical techniques, MFs also have their inherent disadvantages. One of the major difficulties in employing MFs is the problem of domain integration. In fact, Dolbow and Belytschko [16] demonstrated that two primary sources of domain integration errors in MFs are the rational nature of MF shape functions and the misalignment between the shape function supports and integration domains. Both factors affect the accuracy and convergence of numerical solutions.

Satoyuki Tanaka
E-mail: satoyuki@hiroshima-u.ac.jp

[1] Graduate School of Advanced Science and Engineering, Hiroshima University, 4-1, Kagamiyama 1-chome, Higashi-Hiroshima 739-8527, Japan

[2] Duy Tan Research Institute for Computational Engineering (DTRICE), Duy Tan University, Ho Chi Minh City 700000, Vietnam

[3] Faculty of Civil Engineering, Duy Tan University, Da Nang 550000, Viet Nam

In early literature such as Belytschko [1], background cells combined with high-order Gauss quadrature was proposed for numerical integration, and this technique offers the stability and convergence of the solutions. However, the choice of high-order quadrature leads to an expensive integration scheme. It is worth noting that low-order quadrature consumes less computational time but can lead to inaccurate and even non-convergent numerical solutions [17–21]. However, it has been realized by many studies [18–21] that even high-order quadrature may fail the linear patch test, so it affects the overall accuracy and convergence rate of the method.

A viable alternative to the high-order quadrature is the use of nodal integration (NI). At first, it appears that node-based integration is a promising option due to its straightforward implementation and efficiency. However, it turns out that NI is vulnerable to numerical instability which was proven in many works of the early development [17, 18, 22, 23]. After the realization of instability issues, there are several NI techniques that have been proposed to correct the problems. Beissel and Belytschko [17] presented a least-square stabilization in which the original energy functional is augmented by a stabilization term containing the square of the residual of the equilibrium equation. The method successfully suppresses the numerical oscillation, but because of the second derivatives of the displacements included in the formulation, a quadratic basis is required to maintain the consistency, thus resulting in more expensive computations. In the same paper, it was pointed out that the reason for spatial stability is that the integrals of the variational form are only sampled at nodes whose shape function's derivatives are nearly zero, leading to the underestimation of contributions of the strain energy term to the stiffness matrix. Stress point integration was suggested by Dyka et al. [22] to eliminate the oscillations in smoothed-particle hydrodynamics method by taking the derivatives at points away from nodes. Bonet and Kulasegaram [23] introduced a least-square stabilization and an integration correction to remove the spatial stability and pass the linear patch test, hence improving the accuracy.

Chen et al. [18] derived an integration constraint for MFs to satisfy the linear patch test and proposed a stabilized conforming nodal integration method (SCNI) which utilizes the strain smoothing technique to fulfill the integration constraint. Specifically, by the application of the divergence theorem, the strains at nodes are smoothed over conforming cells such that the integration constraint is satisfied, and the derivatives are not directly computed at nodes, which eliminates the spatial instability. Although SCNI can overcome the zero-energy mode due to the zero gradients at nodes, the low-energy modes still exist under certain loading and boundary conditions (BCs). Therefore, additional stabilization is needed to obtain stable solutions for these cases.

Puso et al. [24] proposed a modified stabilized conforming nodal integration method (MSCNI) in which a least-square type stabilization term is added into the stiffness matrix to remove the spurious modes. Wang and Chen [14] presented a subdomain stabilized conforming integration (SSCI) to improve the accuracy and stabilize the oscillatory modes in the context of plates and shells. In this approach, each smoothing cell is further divided into conforming sub-cells, and the strain smoothing operations are performed on these sub-cells. Recently, a fast stabilization technique called naturally stabilized nodal integration (NSNI) was proposed by Hillman [20] to eliminate the spurious modes. The Taylor series expansion is utilized to circumvent the instability, and the second-order derivatives are constructed by the implicit gradient expansion instead of being evaluated directly. Thus, the CPU consumption is significantly reduced, yielding an efficient stabilized method. It should be noted the all SCNI-based methods (SCNI, MSCNI, SSCI, and NSNI) were designed to pass the integration constraint, thus satisfying the linear patch test. The smoothed particle Garlerkin (SPG) method [25,26] is another gradient-based NI introduced to overcome the need of background mesh and provide parameter-free stabilization for non-linear structural analysis. In contrast to SCNI [18] which employs the strain smoothing, the SPG introduces the stabilization effect by means of displacment (or velocity) smoothing.

Another drawback of MFs lies in the approximation properties of MF shape functions which are generally very smooth. It has been known that smooth approximations have difficulty in reproducing functions with non-smooth characteristics, and they exhibit oscillatory behaviour at the line of discontinuity. Such oscillations are the well-known Gibbs phenomenon. In elasticity, an archetype of problems whose solutions are non-smooth is material interface problems in which there is a jump in derivatives of the displacement across the interface.

In the context of MFs, one of the earliest works to tackle the interface problem was published by Cordes and Moran [27]. In their approach, the nodal influence domains that intersect the interface are truncated, and the interface conditions are weakly imposed in the variational form by the Lagrange multipliers. However, the oscillations in stress and strain fields were observed around the interface, so two filtering methods were also proposed to reduce the oscillations. Using the extrinsic enrichment technique, Krongauz and Belytschko [28]

added a global function containing discontinuities in derivatives to the approximation space to capture the jump in strains across the interface, and the jump shape functions were constructed to have compact support so that the discrete equations are banded. Consequently, a considerable improvement in the accuracy of strain solutions is obtained as compared to the standard EFG at the cost of introducing extra degrees of freedom (DOFs) associated with the jump strength.

Based on the enriched function given by Krongauz and Belytschko [28], Wang et al. [29] directly embedded the derivative discontinuities into the basis functions instead of modifying the approximation space to model material interfaces. By the adoption of intrinsic enrichment, this method does not introduce additional DOFs. Liu and Taciroglu [30] then extended the work by Wang et al. [29] to the analysis of homogeneous piezoelectric structures with arbitrarily shaped interfaces that are represented by a set of cubic spline segments. Furthermore, they also studied the effect of support size when using the intrinsic enrichment on the results, and they concluded that a larger support size than the normal one is needed to obtain reasonable solutions. Joyot et al. [31] combined the intrinsic enrichment with the level set method to propose an RK approximation which is capable of reproducing functions with discontinuous derivatives. It is worth mentioning that due to the implicit representation of material interfaces by the level set function, no interface nodes are required. A basis function with built-in discontinuous derivative was presented to replace the standard linear basis function to model the weak discontinuity by Masuda and Noguchi [32].

More recently, a class of immersed MFs has been extensively studied for the analysis of inhomogeneous media by Wu et al. [33], Wang et al. [34], Huang [35], among others. In these immersed methods, each subdomain is independently discretized from one another, so they provide huge potential for resolving problems involved with complicated material interfaces. Another interesting approach is to use the conforming window presented by Koester and Chen [36], in which the window functions are constructed to conform to interface boundaries, enabling a natural reproduction of weak discontinuities in the approximation.

According to the authors' knowledge, available enriched MFs for the interface problems in the literature such as [28–32] primarily consider the background cell with high-order Gauss quadrature as the main integration method. Therefore, the major objective of the present paper is to develop an enriched RKPM in the framework of NI to tackle the interface problems. This is the main novelty of the current study. Specifically, we adopt the local enrichment concept in which an absenrichment function [37] is added to the approximation space to capture the discontinuities in derivatives. Furthermore, the level set method [38] is employed, so it is unnecessary to place nodes on the interface, bypassing the discretization effort required for conforming techniques. In this work, we only focus on the linear elastic analysis. Moreover, we emphasize that our goal is to enhance the accuracy of the standard RKPM in the considered problems, so we do not aim at developing a method that can compete with (extended) FEM in solving such problems.

The remainder of this paper is organized as follows. The construction of meshfree approximation is presented in Section 2 where the RK approximation is focused. In Section 3, the smoothing operation for NI is presented, and the foundation of assumed strain method is introduced in order to cast the smoothed strain into the variational form in Section 4. An enriched RKPM formulated to tackle the interface problems with an emphasis on the combination with NI is presented in Section 5. Finally, several benchmark problems are studied to examine the performance of the proposed methods in Section 6.

2 Reproducing kernel approximation

In MFs, the approximation is constructed based on a set of scattered nodes, which is different from mesh-based methods whose approximation relies on elements. Two popular approaches for constructing approximation in MFs are moving least square (MLS) [1] and reproducing kernel (RK) approximation [2]. In this work, we focus only on the RK approximation to demonstrate the properties of approximation functions commonly used in MFs.

We briefly introduce the multi-index notation. A d-dimensional multi-index is a d-tuple of non-negative integers $\alpha = (\alpha_1, \alpha_2, ..., \alpha_d)$. For a multi-index α and $\boldsymbol{x} = (x_1, \cdots, x_d) \in \mathbb{R}^d$, we define

- Length of α: $|\alpha| = \alpha_1 + \alpha_2 + \cdots + \alpha_d$
- Power: $\boldsymbol{x}^\alpha = x_1^{\alpha_1} x_2^{\alpha_2} \cdots x_d^{\alpha_d}$
- Subscript: $b_\alpha = b_{\alpha_1 \alpha_2 \cdots \alpha_d}$

Consider an open bounded domain $\Omega \subset \mathbb{R}^d$ which is discretized by a set of nodes $\{\boldsymbol{x}_I \in \Omega : 1 \leq I \leq NP\}$, where NP is the number of nodes. Let $u : \Omega \to \mathbb{R}$ be a real-valued function on Ω. Although a real-valued function is considered here for simplicity, the extension to vector-valued functions is straightforward. The RK approximation of the function $u(\boldsymbol{x})$ denoted by $u^h(\boldsymbol{x})$ is constructed by the product of a kernel function $\phi_a(\boldsymbol{x} -$

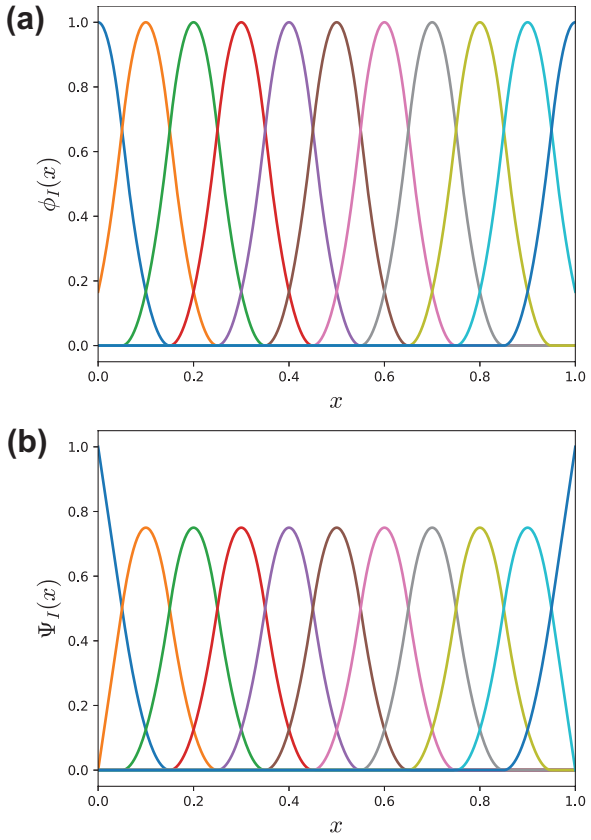

Fig. 1: Cubic B-spline kernel function and corresponding RK shape function with linear basis in one dimension: (a) Kernel function, (b) RK shape function.

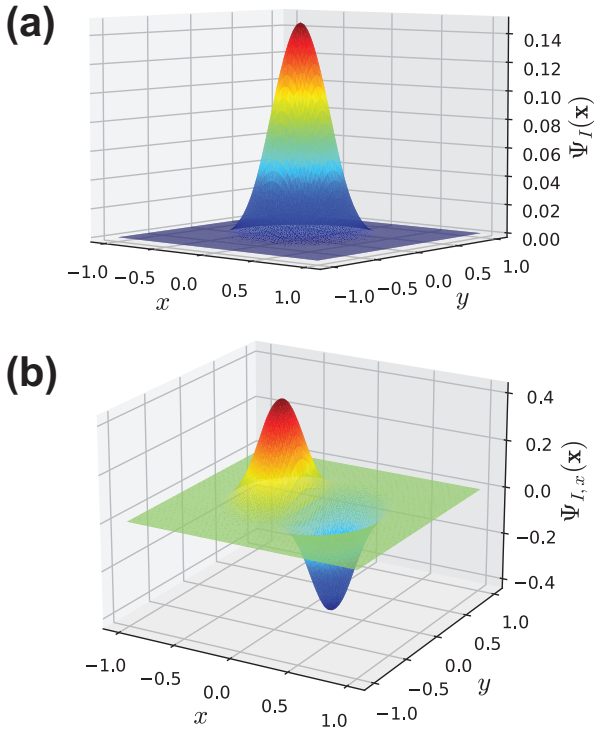

Fig. 2: RK shape function and its x-derivatives with linear basis and cubic B-spline in two dimensions: (a) RK shape function, (b) corresponding x-derivatives.

$\boldsymbol{x}_I$) with compact support and a correction function $C(\boldsymbol{x}, \boldsymbol{x}-\boldsymbol{x}_I)$ as follows

$$u^h(\boldsymbol{x}) = \sum_{I=1}^{NP} C(\boldsymbol{x}, \boldsymbol{x}-\boldsymbol{x}_I)\phi_a(\boldsymbol{x}-\boldsymbol{x}_I)u_I = \sum_{I=1}^{NP} \psi_I(\boldsymbol{x})u_I, \tag{1}$$

where $\psi_I(\boldsymbol{x}) = C(\boldsymbol{x}, \boldsymbol{x}-\boldsymbol{x}_I)\phi_a(\boldsymbol{x}-\boldsymbol{x}_I)$ is the RK shape function, and u_I is the nodal parameter associated with a node I.

The correction function $C(\boldsymbol{x}, \boldsymbol{x}-\boldsymbol{x}_I)$ is constructed such that the RK shape functions satisfy the reproducing conditions. Particularly, the correction function is represented by an n-th order polynomial as

$$C(\boldsymbol{x}, \boldsymbol{x}-\boldsymbol{x}_I) = \sum_{|\alpha|\leq n} b_\alpha(\boldsymbol{x})(\boldsymbol{x}-\boldsymbol{x}_I)^\alpha, \tag{2}$$

in which the set of unknown coefficients $\{b_\alpha(\boldsymbol{x})\}_{|\alpha|\leq n}$ are determined by enforcing the following n-th reproducing conditions

$$\sum_{I=1}^{NP} \psi_I(\boldsymbol{x})\boldsymbol{x}_I^\alpha = \boldsymbol{x}^\alpha, \quad |\alpha| \leq n. \tag{3}$$

Then the RK shape function of a node I, $\psi_I(\boldsymbol{x})$, is expressed as

$$\psi_I(\boldsymbol{x}) = \boldsymbol{H}^T(\boldsymbol{0})\boldsymbol{M}^{-1}(\boldsymbol{x})\boldsymbol{H}(\boldsymbol{x}-\boldsymbol{x}_I)\phi_a(\boldsymbol{x}-\boldsymbol{x}_I), \tag{4}$$

where

$$\boldsymbol{M}(\boldsymbol{x}) = \sum_{I=1}^{NP} \boldsymbol{H}(\boldsymbol{x}-\boldsymbol{x}_I)\boldsymbol{H}^T(\boldsymbol{x}-\boldsymbol{x}_I)\phi_a(\boldsymbol{x}-\boldsymbol{x}_I). \tag{5}$$

In the preceding equation, $\boldsymbol{M}(\boldsymbol{x})$ is the moment matrix, and $\boldsymbol{H}(\boldsymbol{x}-\boldsymbol{x}_I)$ is the basis vector defined as the column vector of $\{(\boldsymbol{x}-\boldsymbol{x}_I)^\alpha\}_{|\alpha|\leq n}$. For example, in one dimension with linear basis

$$\boldsymbol{H}(\boldsymbol{x}-\boldsymbol{x}_I) = [1, x_1 - x_{1I}]^T, \tag{6}$$

in two dimensions with linear basis

$$\boldsymbol{H}(\boldsymbol{x}-\boldsymbol{x}_I) = [1, x_1 - x_{1I}, x_2 - x_{2I}]^T, \tag{7}$$

and in three dimensions with linear basis

$$\boldsymbol{H}(\boldsymbol{x}-\boldsymbol{x}_I) = [1, x_1 - x_{1I}, x_2 - x_{2I}, x_3 - x_{3I}]^T. \tag{8}$$

Note that when the RK shape functions meet the reproducing condition for $n = 0$, they satisfy a crucial property called the **partition of unity**. For shape functions with linear completeness, this property is automatically fulfilled.

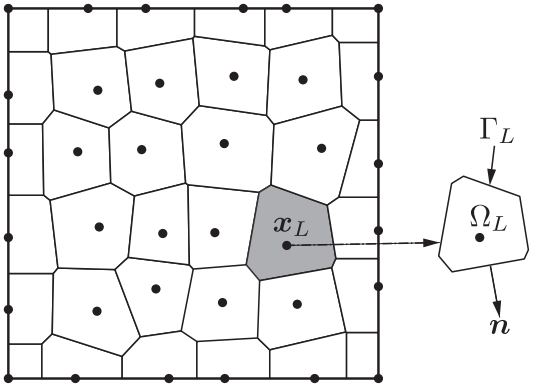

Fig. 3: An example of a square domain discretized by a Voronoi diagram.

A commonly used kernel function is the cubic B-spline function giving C^2 continuity, and it has the following form

$$\phi_a(\boldsymbol{x}-\boldsymbol{x}_I) = \begin{cases} \frac{2}{3} - 4z_I^2 + 4z_I^3 & \text{for} \quad 0 \le z_I \le \frac{1}{2} \\ \frac{4}{3} - 4z_I + 4z_I^2 - \frac{4}{3}z_I^3 & \text{for} \quad \frac{1}{2} \le z_I \le 1 \\ 0 & \text{for} \quad z_I > 1 \end{cases}, \tag{9}$$

where $z_I = \|\boldsymbol{x} - \boldsymbol{x}_I\|/a_I$, and a_I is the support size of the kernel function $\phi_a(\boldsymbol{x} - \boldsymbol{x}_I)$ centered at $\boldsymbol{x}_I$. In this work, we select a_I as follows

$$a_I = ch_I, \tag{10}$$

where we have used $1.5 \le c \le 2.5$ and

$$h_I = \max_{J \in S_J} \|\boldsymbol{x}_J - \boldsymbol{x}_I\|, \tag{11}$$

where S_J is the set of four nodes closest to $\boldsymbol{x}_I$ and different from $\boldsymbol{x}_I$.

Fig. 1 illustrates cubic B-spline function and corresponding RK shape function with linear basis for 11 equispaced nodes in the one-dimensional case.

Fig. 2 shows two-dimensional RK shape function and its x-derivatives with linear basis and cubic B-spline. It is obvious that both shape function and derivatives are smooth because the C^2 kernel function is used.

3 Stabilized conforming nodal integration

In this section, we discuss the smoothed strains used in SCNI proposed by Chen et al. [18]. Basically, the smoothed strains are formulated to meet the following integration constraint [18, 19], which also implies the first-order Galerkin exactness:

$$\overset{\wedge}{\int_\Omega} \nabla\psi_I \, \mathrm{d}V = \overset{\wedge}{\int_\Gamma} \psi_I \, \boldsymbol{n} \, \mathrm{d}\Gamma, \tag{12}$$

where $\wedge$ over the integral sign denotes the numerical integration of domain and boundary integrals, and ψ_I is a shape function with first-order completeness.

Following the concept of SCNI [18], we define the smoothed (or assumed) strain field $\tilde{\boldsymbol{\varepsilon}}$ as follows. Let $\{\boldsymbol{x}_L\}_{L=1}^{NP}$ be the set of nodes used to discretize the domain Ω. Then, by the Voronoi diagram, the domain Ω is discretized into NP subdomains (cells) Ω_L with a boundary Γ_L so that $\Omega = \bigcup_{L=1}^{NP} \Omega_L$, and $\Omega_I \cap \Omega_J = \emptyset$, $\forall I \neq J$, i.e., they do not overlap. Each Ω_L is regarded as the nodal representative domain for the corresponding node $\boldsymbol{x}_L$ as illustrated in Fig. 3. In each subdomain Ω_L, we can subdivide it further into NSC conforming subcells Ω_L^K, i.e., $\Omega_L = \bigcup_{K=1}^{NSC} \Omega_L^K$ as shown in Fig. 4. Note that, in the prsent paper, new subcells are formed by connecting the centroid of a nodal cell to its vertices. For other subdivision schemes, please refer to [14, 21]. Given a displacement field $\boldsymbol{u}$, the assumed strain $\tilde{\boldsymbol{\varepsilon}}$ is constructed on each subcell Ω_L^K as follows:

$$\tilde{\boldsymbol{\varepsilon}}(\boldsymbol{x}_L^K) = \frac{1}{A_L^K} \int_{\Omega_L^K} \boldsymbol{\varepsilon}(\boldsymbol{u}) \, dV, \tag{13}$$

where $\boldsymbol{x}_L^K$ and A_L^K are the centroid of the K-subcell in the L-th nodal cell and the area of Ω_L^K, respectively, and $\boldsymbol{\varepsilon}$ is the infinitesimal strain tensor which is determined by the strain-displacement relations:

$$\boldsymbol{\varepsilon}(\boldsymbol{u}) = \frac{1}{2}(\nabla\boldsymbol{u} + \nabla\boldsymbol{u}^T). \tag{14}$$

Note that the strain $\boldsymbol{\varepsilon}$ which is defined in Eq. (14) is compatible with the displacement field $\boldsymbol{u}$. In contrast, the smoothed strain in Eq. (13) is generally incompatible with the displacement field $\boldsymbol{u}$.

Remark: The assumed strain $\tilde{\boldsymbol{\varepsilon}}(\boldsymbol{x}_L^K)$ given by Eq. (13) is constant in Ω_L^K, and it can be regarded as the smoothing (average) of the compatible strain $\boldsymbol{\varepsilon}(\boldsymbol{u})$ over the subcell Ω_L^K. If the cell Ω_L is not subdivided, the strain smoothing at the given cell is carried out as

$$\tilde{\boldsymbol{\varepsilon}}(\boldsymbol{x}_L) = \frac{1}{A_L} \int_{\Omega_L} \boldsymbol{\varepsilon}(\boldsymbol{u}) \, dV, \tag{15}$$

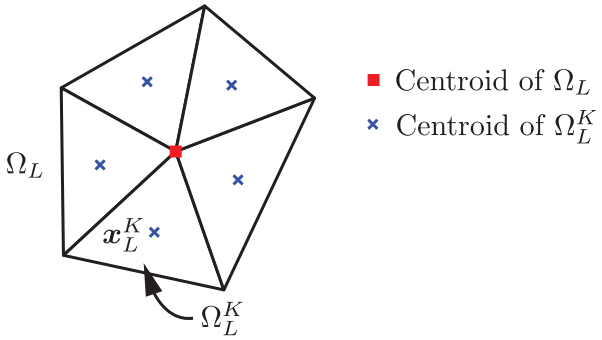

Fig. 4: Schematic illustration of cell subdivision. New subcells are created by connecting the centroid of a nodal cell to its vertices.

where A_L is the area of Ω_L.

Although SCNI can eliminate zero-energy modes by avoiding directly sampling gradients at nodes, in some cases spurious low-energy modes can be excited [20,24]. Therefore, several stabilized techniques for NI were proposed to address the unstable modes such as MSCNI [24], SSCI [14], and NSNI [20]. In this study, SSCI is adopted because it naturally fits in with the cell partitioning strategy discussed later in 5.2.

4 Variational formulation

4.1 Strong form

Consider an open and bounded domain $\Omega \subset \mathbb{R}^2$ with a closed boundary Γ as shown in Fig. 5(a). The boundary Γ consists of two parts Γ_u and Γ_t where $\Gamma_u \cap \Gamma_t = \emptyset$ and $\Gamma_u \cup \Gamma_t = \Gamma$. The strong form of a linear elasticity problem asks to find the displacement field $\boldsymbol{u} : \Omega \to \mathbb{R}^2$ such that the field equations

$$\nabla \cdot \boldsymbol{\sigma} + \boldsymbol{b} = \boldsymbol{0} \quad \text{in } \Omega, \tag{16}$$

subjected to the BCs

$$\boldsymbol{u} = \bar{\boldsymbol{u}} \quad \text{on } \Gamma_u, \tag{17a}$$

$$\boldsymbol{\sigma} \cdot \boldsymbol{n} = \bar{\boldsymbol{t}} \quad \text{on } \Gamma_t, \tag{17b}$$

are satisfied. In Eq. (16) above, $\boldsymbol{\sigma}$ denotes the Cauchy stress tensor, and $\boldsymbol{b}$ is the body force. On the right-hand sides of Eqs. (17a) and (17b), $\bar{\boldsymbol{u}}$ and $\bar{\boldsymbol{t}}$ are the prescribed values of displacement and traction on Γ_u and Γ_t, respectively, and $\boldsymbol{n} = (n_1, n_2)$ is the outward unit normal vector to the boundary Γ. Furthermore, the constitutive law for linear elasticity states

$$\boldsymbol{\sigma} = \mathbb{C} : \boldsymbol{\varepsilon}, \tag{18}$$

where $\mathbb{C}$ is the elasticity tensor.

If there exists a material interface Γ_d in the body, the body is separated into Ω^+ and Ω^- corresponding to $\mathbb{C}^+$ and $\mathbb{C}^-$ with $\Omega = \Omega^+ \cup \Omega^-$ as depicted in Fig. 5(b). Moreover, additional interface conditions are introduced, i.e., continuity of displacement and traction, as follows

$$[[\boldsymbol{u}(\boldsymbol{x})]] = \boldsymbol{u}^+ - \boldsymbol{u}^- = \boldsymbol{0} \quad \text{on } \Gamma_d, \tag{19}$$

$$[[\boldsymbol{\sigma}(\boldsymbol{x}) \cdot \boldsymbol{n}(\boldsymbol{x})]] = \boldsymbol{\sigma}^+ \cdot \boldsymbol{n}^- - \boldsymbol{\sigma}^- \cdot \boldsymbol{n}^- = \boldsymbol{0} \quad \text{on } \Gamma_d, \tag{20}$$

where the subscripts $+$ and $-$ indicate quantities corresponding to Ω^+ and Ω^- as shown in Fig. 5(b).

4.2 Weak form

In order to introduce the smoothed strains presented in Section 3 into the framework of variational formulation, the assumed strain method [39,40] is adopted to derive the following weak form

$$\begin{aligned} &\int_\Omega \delta\tilde{\boldsymbol{\varepsilon}}^h : \mathbb{C} : \tilde{\boldsymbol{\varepsilon}}^h \, dV - \int_{\Gamma_u} \delta\boldsymbol{u}^h \cdot \boldsymbol{t}^h \, dS \\ &- \int_{\Gamma_u} \delta\boldsymbol{t}^h \cdot (\boldsymbol{u}^h - \bar{\boldsymbol{u}}) \, dS + \alpha \int_{\Gamma_u} \delta\boldsymbol{u}^h \cdot (\boldsymbol{u}^h - \bar{\boldsymbol{u}}) \, dS \\ &= \int_\Omega \delta\boldsymbol{u}^h \cdot \boldsymbol{b} \, dV + \int_{\Gamma_t} \delta\boldsymbol{u}^h \cdot \bar{\boldsymbol{t}} \, dS, \end{aligned} \tag{21}$$

where α is a penalty parameter. A detailed derivation of the weak form is given in Appendix A. By inspection, Eq. (21) has a similar form to the Nitsche's method [41] except the compatible strains replaced by the smoothed strains. On the left-hand side of Eq. (21), the second, third and fourth terms are responsible for imposing the essential BCs.

5 Enriched RKPM

In this section, an enriched RKPM method combined with the stabilized NI is proposed to solve material interface problems. To illustrate the difficulties of general MFs in solving such problems, consider a simple problem where a bar composed of two different materials is fixed on one end and is subject to a prescribed unit displacement in the horizontal direction on the other end. In this problem, due to the material discontinuity, there is a jump in strains at the interface.

Fig. 6 depicts the strain solution obtained by the standard RKPM without any special treatment, and unsurprisingly the solution is highly oscillatory and considerably differs from the exact one. In addition, the result given by the proposed method in this section is presented for comparison, and the weak discontinuity is accurately represented. Therefore, a special technique

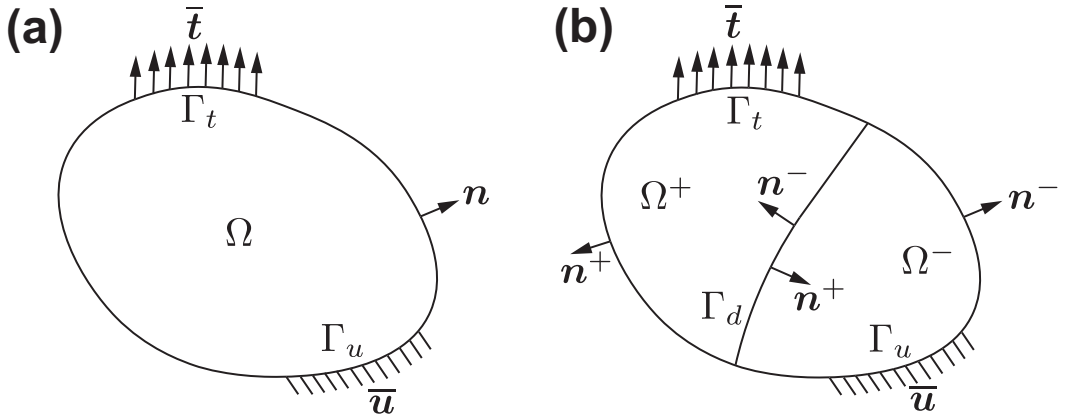

Fig. 5: Domain description: (a) Homogeneous body, (b) Inhomogeneous body.

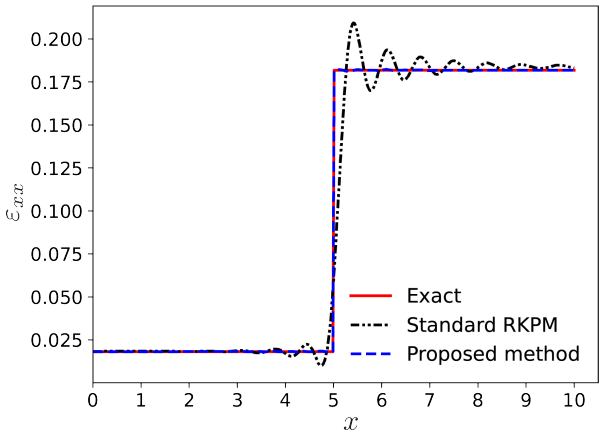

Fig. 6: Strain jump at the material interface located at $x = 5$ for the inhomogeneous bar. The ratio of Young's modulus of the two materials is set to be 10 in this example.

is required to reduce the oscillation and to improve the approximation quality of MF functions in the aforementioned problem. In this paper, we introduce a technique based on the partition of unity property of MF functions.

5.1 Formulation

As discussed in Section 2, the MF shape functions fulfill the partition of unity, so we can enrich the approximation space by an enrichment function which can capture a known feature of the solution. In the present discussion, we assume that there is only one material interface Γ_d in the domain Ω in order to simplify the formulation. However, the extension to multiple interfaces can be done in a similar fashion. For the problem of interest, in addition to the standard MF shape functions, we introduce an enriched function whose derivatives are discontinuous at the interface to the approximation space. As a result, the discrete displacement field, $\boldsymbol{u}^h$, and its variation, $\delta\boldsymbol{u}^h$, can be expressed as

$$\begin{aligned}\boldsymbol{u}^h(\boldsymbol{x}) &= \sum_{I\in G}\psi_I(\boldsymbol{x})\boldsymbol{d}_I + \sum_{J\in M}\psi_J(\boldsymbol{x})\varphi(\boldsymbol{x})\boldsymbol{a}_J \\ &= \boldsymbol{N}_d(\boldsymbol{x})\boldsymbol{d} + \boldsymbol{N}_a(\boldsymbol{x})\boldsymbol{a}, \qquad (22a)\\ \delta\boldsymbol{u}^h(\boldsymbol{x}) &= \sum_{I\in G}\psi_I(\boldsymbol{x})\delta\boldsymbol{d}_I + \sum_{J\in M}\psi_J(\boldsymbol{x})\varphi(\boldsymbol{x})\delta\boldsymbol{a}_J \\ &= \boldsymbol{N}_d(\boldsymbol{x})\delta\boldsymbol{d} + \boldsymbol{N}_a(\boldsymbol{x})\delta\boldsymbol{a}, \qquad (22b)\end{aligned}$$

where G denotes the set of all NP nodes, M is the set of NE nodes whose supports intersect the interface Γ_d, and $\varphi(\boldsymbol{x})$ is the enrichment function.

Furthermore, $\boldsymbol{d} = [\boldsymbol{d}_1, \cdots, \boldsymbol{d}_{NP}]^T$ is the vector of standard DOFs consisting of the nodal vectors of standard DOFs $\boldsymbol{d}_I = [d_{1I}, d_{2I}]^T$ and $\boldsymbol{a} = [\boldsymbol{a}_1, \cdots, \boldsymbol{a}_{NE}]^T$ is the vector of enriched DOFs consisting of the nodal vectors of enriched DOFs $\boldsymbol{a}_J = [a_{1J}, a_{2J}]^T$; $\boldsymbol{N}_d(\boldsymbol{x}) = [\boldsymbol{N}_{d1}(\boldsymbol{x}), \cdots, \boldsymbol{N}_{dNP}(\boldsymbol{x})]$ is the standard shape function matrix composed of the nodal sub-matrix

$$\boldsymbol{N}_{dI}(\boldsymbol{x}) = \begin{bmatrix}\psi_I(\boldsymbol{x}) & 0\\ 0 & \psi_I(\boldsymbol{x})\end{bmatrix}, \qquad (23)$$

and $\boldsymbol{N}_a(\boldsymbol{x}) = [\boldsymbol{N}_{a1}(\boldsymbol{x}), \cdots, \boldsymbol{N}_{aNE}(\boldsymbol{x})]$ is the enriched shape function matrix composed of the nodal sub-matrix

$$\boldsymbol{N}_{aJ}(\boldsymbol{x}) = \begin{bmatrix}\hat{\psi}_J(\boldsymbol{x}) & 0\\ 0 & \hat{\psi}_J(\boldsymbol{x})\end{bmatrix}, \qquad (24)$$

where $\hat{\psi}_J(\boldsymbol{x}) \coloneqq \psi_J(\boldsymbol{x})\varphi(\boldsymbol{x})$.

In this work, the enrichment function $\varphi(\boldsymbol{x})$ used to capture weak discontinuities is the abs-enrichment [37] which is defined as

$$\varphi(\boldsymbol{x}) = |\phi(\boldsymbol{x})| = \begin{cases} -\phi(\boldsymbol{x}) & \text{if} \quad \phi(\boldsymbol{x}) < 0 \\ +\phi(\boldsymbol{x}) & \text{if} \quad \phi(\boldsymbol{x}) \geq 0 \end{cases}, \qquad (25)$$

in which $\phi(\boldsymbol{x}) : \Omega \to \mathbb{R}$ is the signed distance function defined to represent the interface position by

$$\phi(\boldsymbol{x}) = \pm \min_{\boldsymbol{x}^* \in \Gamma_d} \|\boldsymbol{x} - \boldsymbol{x}^*\|, \tag{26}$$

where the sign is different on two sides of the interface Γ_d. It should be noted that an enriched node has more DOFs than a standard node. For each interface cut by the support of a node $\boldsymbol{x}_L$, two additional enriched DOFs are added to that node. For example, if a node $\boldsymbol{x}_L$ has its support cut only one interface, it will have four DOFs instead of two.

With the addition of the enrichment to the displacement approximation, the smoothed strain vector can be found as follows,

$$\begin{aligned}
&\tilde{\varepsilon}^h_{ij}(\boldsymbol{x}^K_L) \\
&= \frac{1}{A^K_L}\int_{\Omega^K_L} \varepsilon_{ij}(\boldsymbol{u}^h)\, dV \\
&= \frac{1}{2A^K_L}\int_{\Omega^K_L} [u^h_{i,j}(\boldsymbol{x}) + u^h_{j,i}(\boldsymbol{x})]\, dV \\
&= \frac{1}{2A^K_L}\int_{\Gamma^K_L} [u^h_i(\boldsymbol{x})n_j(\boldsymbol{x}) + u^h_j(\boldsymbol{x})n_i(\boldsymbol{x})]\, dS \\
&\quad \text{(by the divergence theorem)} \\
&= \sum_{I\in G} \frac{1}{2A^K_L}\int_{\Gamma^K_L} [\psi_I(\boldsymbol{x})n_j(\boldsymbol{x})d_{iI} + \psi_I(\boldsymbol{x})n_i(\boldsymbol{x})d_{jI}]\, dS \\
&+ \sum_{J\in M} \frac{1}{2A^K_L}\int_{\Gamma^K_L} [\hat{\psi}_J(\boldsymbol{x})n_j(\boldsymbol{x})a_{iJ} + \hat{\psi}_J(\boldsymbol{x})n_i(\boldsymbol{x})a_{jJ}]\, dS,
\end{aligned}$$

where $\boldsymbol{x}^K_L$ is the centroid of the K-subcell in the L-th nodal cell, and A^K_L is the corresponding area of that K-th subcell.

The smoothed strain vector, $\tilde{\boldsymbol{\varepsilon}}^h(\boldsymbol{x}^K_L)$, and its variation, $\delta\tilde{\boldsymbol{\varepsilon}}^h(\boldsymbol{x}^K_L)$, are given in the matrix form as

$$\begin{aligned}
\tilde{\boldsymbol{\varepsilon}}^h(\boldsymbol{x}^K_L) &= \sum_{I\in G} \tilde{\boldsymbol{B}}^d_I(\boldsymbol{x}^K_L)\boldsymbol{d}_I + \sum_{J\in M} \tilde{\boldsymbol{B}}^a_J(\boldsymbol{x}^K_L)\boldsymbol{a}_J \\
&= \tilde{\boldsymbol{B}}_d(\boldsymbol{x}^K_L)\boldsymbol{d} + \tilde{\boldsymbol{B}}_a(\boldsymbol{x}^K_L)\boldsymbol{a}, \qquad (27a) \\
\delta\tilde{\boldsymbol{\varepsilon}}^h(\boldsymbol{x}^K_L) &= \sum_{I\in G} \tilde{\boldsymbol{B}}^d_I(\boldsymbol{x}^K_L)\delta\boldsymbol{d}_I + \sum_{J\in M} \tilde{\boldsymbol{B}}^a_J(\boldsymbol{x}^K_L)\delta\boldsymbol{a}_J \\
&= \tilde{\boldsymbol{B}}_d(\boldsymbol{x}^K_L)\delta\boldsymbol{d} + \tilde{\boldsymbol{B}}_a(\boldsymbol{x}^K_L)\delta\boldsymbol{a}, \qquad (27b)
\end{aligned}$$

where the standard smoothed gradient matrix $\tilde{\boldsymbol{B}}_d(\boldsymbol{x}^K_L) = [\tilde{\boldsymbol{B}}_{d1}(\boldsymbol{x}^K_L), \cdots, \tilde{\boldsymbol{B}}_{dNP}(\boldsymbol{x}^K_L)]$, and the standard nodal submatrix,

$$\tilde{\boldsymbol{B}}_{dI}(\boldsymbol{x}^K_L) = \begin{bmatrix} \tilde{\psi}_{I,1}(\boldsymbol{x}^K_L) & 0 \\ 0 & \tilde{\psi}_{I,2}(\boldsymbol{x}^K_L) \\ \tilde{\psi}_{I,2}(\boldsymbol{x}^K_L) & \tilde{\psi}_{I,1}(\boldsymbol{x}^K_L) \end{bmatrix}, \tag{28}$$

where

$$\tilde{\psi}_{I,i}(\boldsymbol{x}^K_L) = \frac{1}{A^K_L}\int_{\Gamma^K_L} \psi_I(\boldsymbol{x})n_i(\boldsymbol{x})\, dS, \tag{29}$$

and the enriched smoothed gradient matrix $\tilde{\boldsymbol{B}}_a(\boldsymbol{x}^K_L) = [\tilde{\boldsymbol{B}}_{a1}(\boldsymbol{x}^K_L), \cdots, \tilde{\boldsymbol{B}}_{aNE}(\boldsymbol{x}^K_L)]$, and the enriched nodal submatrix

$$\tilde{\boldsymbol{B}}_{aJ}(\boldsymbol{x}^K_L) = \begin{bmatrix} \tilde{\psi}_{J,1}(\boldsymbol{x}^K_L) & 0 \\ 0 & \tilde{\psi}_{J,2}(\boldsymbol{x}^K_L) \\ \tilde{\psi}_{J,2}(\boldsymbol{x}^K_L) & \tilde{\psi}_{J,1}(\boldsymbol{x}^K_L) \end{bmatrix}, \tag{30}$$

where

$$\tilde{\psi}_{J,i}(\boldsymbol{x}^K_L) = \frac{1}{A^K_L}\int_{\Gamma^K_L} \hat{\psi}_J(\boldsymbol{x})n_i(\boldsymbol{x})\, dS. \tag{31}$$

In order to obtain the discrete equation from the variational form, plugging Eqs. (22) and (27) into Eq. (21) yields

$$\delta\boldsymbol{d}^T(\boldsymbol{K}^{dd}\boldsymbol{d}+\boldsymbol{K}^{da}\boldsymbol{a}-\boldsymbol{F}^d)+\delta\boldsymbol{a}^T(\boldsymbol{K}^{ad}\boldsymbol{d}+\boldsymbol{K}^{aa}\boldsymbol{a}-\boldsymbol{F}^a) = 0.$$

By invoking the arbitrariness of variation vectors, $\delta\boldsymbol{d}$ and $\delta\boldsymbol{a}$, the discrete equations for Eq. (21) are

$$\begin{bmatrix} \boldsymbol{K}^{dd} & \boldsymbol{K}^{da} \\ \boldsymbol{K}^{ad} & \boldsymbol{K}^{aa} \end{bmatrix} \begin{bmatrix} \boldsymbol{d} \\ \boldsymbol{a} \end{bmatrix} = \begin{bmatrix} \boldsymbol{F}^d \\ \boldsymbol{F}^a \end{bmatrix}, \tag{32}$$

where

$$\begin{aligned}
\boldsymbol{K}^{\alpha\beta} &= \int_\Omega \tilde{\boldsymbol{B}}^T_\alpha \boldsymbol{D}\tilde{\boldsymbol{B}}_\beta\, dV - \int_{\Gamma_u} \boldsymbol{N}^T_\alpha \boldsymbol{S}^T\boldsymbol{G}^T\boldsymbol{D}\tilde{\boldsymbol{B}}_\beta\, dS \\
&\quad - \int_{\Gamma_u} \tilde{\boldsymbol{B}}^T_\alpha \boldsymbol{D}\boldsymbol{G}\boldsymbol{S}\boldsymbol{N}_\beta\, dS + \alpha\int_{\Gamma_u} \boldsymbol{N}^T_\alpha \boldsymbol{S}\boldsymbol{N}_\beta\, dS, \qquad (33)
\end{aligned}$$

$$\begin{aligned}
\boldsymbol{F}^\alpha &= \int_\Omega \boldsymbol{N}^T_\alpha \boldsymbol{b}\, dV + \int_{\Gamma_t} \boldsymbol{N}^T_\alpha \bar{\boldsymbol{t}}\, dS + \alpha\int_{\Gamma_u} \boldsymbol{N}^T_\alpha \boldsymbol{S}\bar{\boldsymbol{u}}\, dS \\
&\quad - \int_{\Gamma_u} \tilde{\boldsymbol{B}}^T_\alpha \boldsymbol{D}\boldsymbol{G}\boldsymbol{S}\bar{\boldsymbol{u}}\, dS, \qquad (34)
\end{aligned}$$

where $\alpha, \beta \in \{d, a\}$ and for plane stress,

$$\boldsymbol{D} = \frac{E}{1-\nu^2}\begin{bmatrix} 1 & \nu & 0 \\ \nu & 1 & 0 \\ 0 & 0 & \frac{1-\nu}{2} \end{bmatrix}, \tag{35}$$

and for plane strain,

$$\boldsymbol{D} = \frac{E}{(1+\nu)(1-2\nu)}\begin{bmatrix} 1-\nu & \nu & 0 \\ \nu & 1-\nu & 0 \\ 0 & 0 & \frac{1-2\nu}{2} \end{bmatrix}. \tag{36}$$

$$\boldsymbol{G} = \begin{bmatrix} n_1 & 0 \\ 0 & n_2 \\ n_2 & n_1 \end{bmatrix}, \tag{37}$$

$$\boldsymbol{S} = \begin{bmatrix} s_x & 0 \\ 0 & s_y \end{bmatrix}, \tag{38}$$

and

$$s_x = \begin{cases} 1, & \text{if prescribed } u_x \text{ on } \Gamma_u \\ 0, & \text{if prescribed } u_y \text{ on } \Gamma_u \end{cases}, \tag{39}$$

$$s_y = \begin{cases} 1, & \text{if prescribed } u_y \text{ on } \Gamma_u \\ 0, & \text{if prescribed } u_x \text{ on } \Gamma_u \end{cases}, \tag{40}$$

in which E and ν are Young's modulus and Poisson's ratio, respectively. Note that the coefficient matrix in Eq. (32) is symmetric.

The stiffness matrix $\boldsymbol{K}^{\alpha\beta}$ and force vector $\boldsymbol{F}^{\alpha}$ are assembled from 2×2 sub-matrices $\boldsymbol{K}_{IJ}^{\alpha\beta}$ and 2×1 sub-matrices $\boldsymbol{F}_{I}^{\alpha}$ given by

$$\begin{aligned}\boldsymbol{K}_{IJ}^{\alpha\beta} = &\int_{\Omega} \tilde{\boldsymbol{B}}_{\alpha I}^{T}\boldsymbol{D}\tilde{\boldsymbol{B}}_{\beta J}\,dV - \int_{\Gamma_u} \boldsymbol{N}_{\alpha I}^{T}\boldsymbol{S}^{T}\boldsymbol{G}^{T}\boldsymbol{D}\tilde{\boldsymbol{B}}_{\beta J}\,dS \\ &- \int_{\Gamma_u} \tilde{\boldsymbol{B}}_{\alpha I}^{T}\boldsymbol{D}\boldsymbol{G}\boldsymbol{S}\boldsymbol{N}_{\beta J}\,dS + \alpha\int_{\Gamma_u} \boldsymbol{N}_{\alpha I}^{T}\boldsymbol{S}\boldsymbol{N}_{\beta J}\,dS,\end{aligned} \tag{41}$$

$$\begin{aligned}\boldsymbol{F}_{I}^{\alpha} = &\int_{\Omega} \boldsymbol{N}_{\alpha I}^{T}\boldsymbol{b}\,dV + \int_{\Gamma_t} \boldsymbol{N}_{\alpha I}^{T}\bar{\boldsymbol{t}}\,dS + \alpha\int_{\Gamma_u} \boldsymbol{N}_{\alpha I}^{T}\boldsymbol{S}\bar{\boldsymbol{u}}\,dS \\ &- \int_{\Gamma_u} \tilde{\boldsymbol{B}}_{\alpha I}^{T}\boldsymbol{D}\boldsymbol{G}\boldsymbol{S}\bar{\boldsymbol{u}}\,dS.\end{aligned} \tag{42}$$

5.2 Enrichment strategy and numerical integration

We present a strategy to determine enriched nodes and carry out numerical integration for material interface problems.

The level set function $\phi(\boldsymbol{x})$ is utilized as a local enrichment as well as describing the interface location. We employ the level set function to determine cells intersected by an interface and nodes that need to be enriched. Firstly we loop over each cell in the domain. For each cell Ω_L, we compute the level set value ϕ_I at each vertex v_I of the cell. If there exists two vertices, v_I and v_J, of the cell such that $\phi_I\phi_J < 0$, then the cell Ω_L is cut and the corresponding node $\boldsymbol{x}_L$ is enriched.

For numerical integration, we need to take into account the partition of cells cut by the interface to carry out the first integral in Eq. (41), which involves the elasticity matrix. For cut cells, they must be sub-divided into subcells that conform to the interface and possess constant material properties. Assume that the interface intersects two edges of a cell, each of which contains vertices whose level set values have opposite signs, as depicted in Fig. 7(a). On each of the two edges, we need to locate the intersection between the interface and the cell edges, i.e. points where $\phi(\boldsymbol{x}) = 0$. Here we use linear interpolation based on the level set values at the vertices of the edge to determine these points (red squares in Fig. 7(b)). Afterwards, we connect two newly-identified points to create two subcells, and we further subdivide these subcells into other subcells as shown in Fig. 7(c).

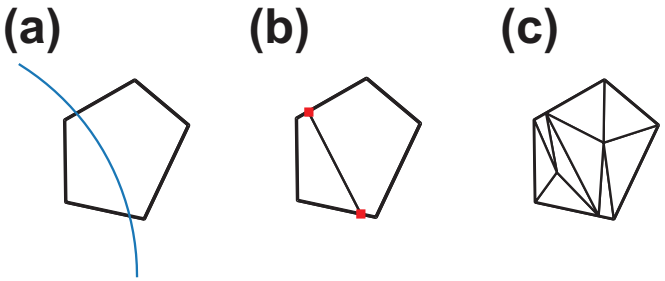

Fig. 7: Partitioning scheme for numerical integration: (a) A cell cut by an interface denoted by a blue curve, (b) Identification of the intersections between the interface and cell edges denoted by red squares and the creation of two new subcells, (c) Further subdivision of newly-created subcells.

By employing SSCI [14], the first term of Eq. (41) can be discretized as,

$$\int_{\Omega} \tilde{\boldsymbol{B}}_{\alpha I}^{T}\boldsymbol{D}\tilde{\boldsymbol{B}}_{\beta J}\,dV \approx \sum_{L=1}^{NP}\sum_{K=1}^{NSC} \tilde{\boldsymbol{B}}_{\alpha I}^{T}(\boldsymbol{x}_L^K)\boldsymbol{D}\tilde{\boldsymbol{B}}_{\beta J}(\boldsymbol{x}_L^K)\,A_L^K, \tag{43}$$

in which NSC denotes the number of sub-cells associated with the L-th nodal cell, and D is the appropriate elasticity matrix. Except cut cells, other cells can be partitioned in the same manner as illustrated in Fig. 4. For evaluation of the contour integrals in Eqs. (29) and (31), one-point Gauss integration rule [19] is used per edge of a (sub-)cell. Additionally, the same integral quadrature rule is employed for the boundary terms in Eqs. (41) and (42).

6 Numerical examples

Several numerical examples are examined to study the performance of the proposed method. The RK approximation with linear basis and cubic B-spline kernel is employed, and the normalized support size $c = 2.5$ is chosen. The penalty parameter α in Eqs. (33) and (34) is chosen as suggested by [41], i.e., $\alpha = \beta(E/h)$ where β is the normalized penalty parameter, and h is the characteristic nodal spacing. Herein, h is the maximum nodal spacing, and the normalized penalty parameter $\beta = 100$ is used. In the following examples, RKPM

is used to denote the standard RKPM combined with SSCI, and ERKPM represents the enriched RKPM with SSCI. In the above methods, proper cell subdivision introduced in Section 5.2 was performed.

For the error evaluation, the standard error norms, L_2 norm and energy norm, are adopted:

$$\|\boldsymbol{u}^h - \boldsymbol{u}^e\|_{L_2} = \sqrt{\frac{\int_\Omega (\boldsymbol{u}^h - \boldsymbol{u}^e)^T (\boldsymbol{u}^h - \boldsymbol{u}^e)\, dV}{\int_\Omega (\boldsymbol{u}^e)^T (\boldsymbol{u}^e)\, dV}}, \tag{44}$$

$$\|\boldsymbol{u}^h - \boldsymbol{e}^h\|_E = \sqrt{\frac{\int_\Omega (\boldsymbol{\varepsilon}^h - \boldsymbol{\varepsilon}^e)^T \boldsymbol{D} (\boldsymbol{\varepsilon}^h - \boldsymbol{\varepsilon}^e)\, dV}{\int_\Omega (\boldsymbol{\varepsilon}^e)^T \boldsymbol{D} (\boldsymbol{\varepsilon}^e)\, dV}}, \tag{45}$$

where $(\boldsymbol{u}^h, \boldsymbol{\varepsilon}^h)$ and $(\boldsymbol{u}^e, \boldsymbol{\varepsilon}^e)$ denote numerical and exact solutions, respectively. The error norm calculations for Eqs. (44) and (45) are carried out using 37-point quadrature [42] in each triangular subcell. Moreover, the convergence rate, R, of each formulation is obtained by linear regression.

Furthermore, in order to create non-uniform discretization, we displace nodes in the uniform grid by a random amount by the below formula:

$$x' = x + (2r_c - 1)\beta_{irr}\Delta x, \tag{46}$$

$$y' = y + (2r_c - 1)\beta_{irr}\Delta y, \tag{47}$$

where (x, y) is the initial coordinates in the uniform grid, r_c is the random number in the interval $[0, 1]$, Δx and Δy are uniform nodal spacing, and β_{irr} is a factor that controls the irregularity of nodal distribution.

6.1 Bi-material plate

A two-dimensional plate is composed of two linear elastic materials with Young's moduli of $E_1 = 10$, $E_2 = 1$ and Poisson's ratios of $\nu_1 = \nu_2 = 0$. The length and width of the plate are 10 and 2, respectively. The material interface is placed at $x = 5$. The plate is fixed on one end and subject to a prescribed displacement on the other end, see Fig. 8.

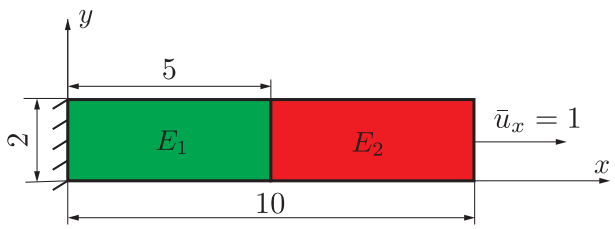

Fig. 8: Bi-material plate subject to body force.

Two cases are considered:

– A linear body force $\boldsymbol{b}(\boldsymbol{x}) = x$ is applied.

– A nonlinear body force $\boldsymbol{b}(\boldsymbol{x}) = 25x - 7.5x^2 + 0.5x^3$ is applied.

Since the Poisson's ratio is set to 0, the exact solution to this problem is the same as one for one dimension. The analytical solution to the one-dimensional case can be found in [27].

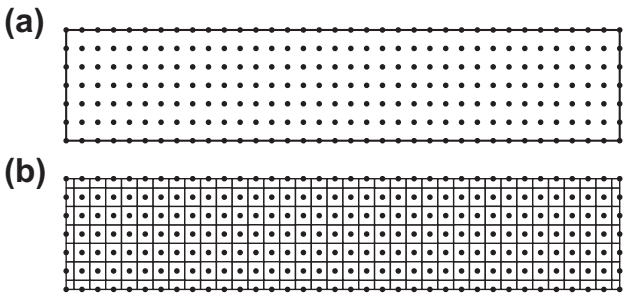

Fig. 9: A 36×7 discretization for the bi-material plate: (a) Nodal distribution, (b) Corresponding Voronoi diagram.

For the convergence study, we consider different uniform discretization: 36×7, 46×9, 56×11, 66×13, and 76×15. Fig. 9 shows 36×7 discretization and the corresponding Voronoi diagram. Here there are no nodes required on the material interface. For the first case where the linear body force is applied, the convergence in L_2 norm and energy norm is illustrated in Fig. 10. Obviously, not only accuracy but also convergence behaviour is considerably improved by ERKPM as compared with the standard RKPM. With the added enrichment, the convergence rates obtained by ERKPM in L_2 and energy norms are close to the optimal ones (2 in L_2 norm and 1 in energy norm), whereas the convergence rates of RKPM are reduced by half in both norms because of non-smooth behaviour of solutions.

The comparison of displacement and strain computed by ERKPM and RKPM for 36×7 grid are given in Figs. 11 and 12. While ERKPM can capture well the jump in strains at the interface, the strains obtained by pure RKPM are highly oscillatory around the discontinuity, hence degrading the overall accuracy. Furthermore, the same problem is solved for a homogeneous plate ($E_1/E_2 = 1$), and the convergence rates are shown in Fig. 13. In L_2 norm, ERKPM and RKPM produce identical convergence rate and accuracy, whereas ERKPM is slightly less accurate than RKPM but having similar convergence rate in the energy norm.

For the second case where the non-linear body force is imposed, the convergence behaviour in L_2 norm and energy norm are shown in Fig. 14. As can be seen from the figures, the accuracy and convergence rates of

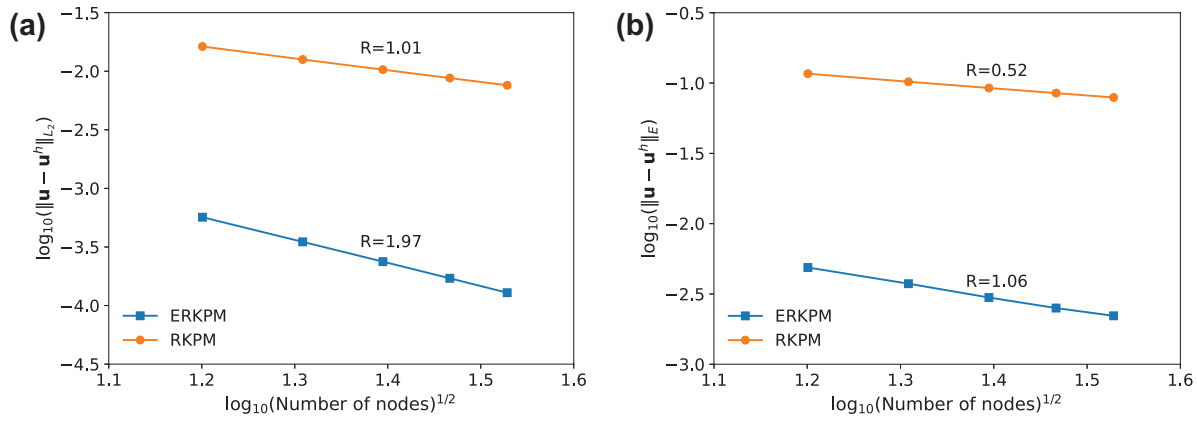

Fig. 10: Convergence results for the bi-material plate subject to a linear body force: (a) L_2 norm, (b) Energy norm.

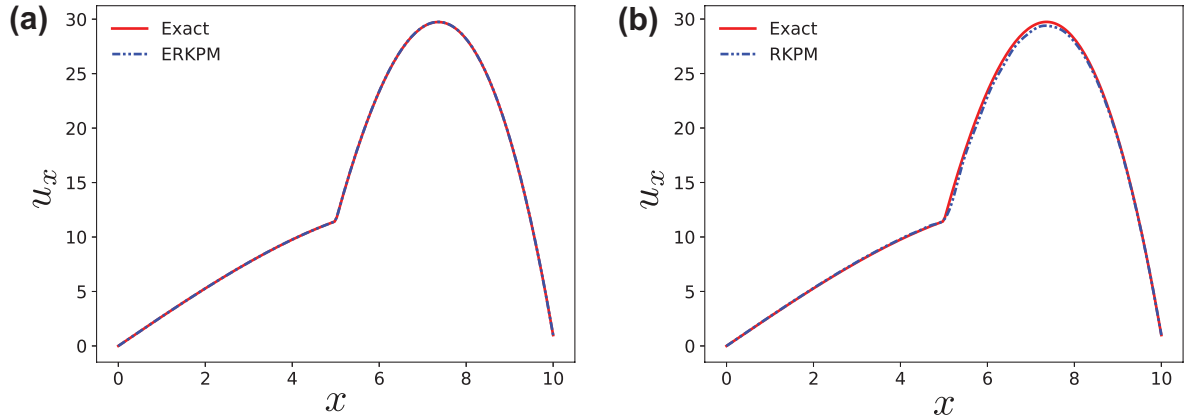

Fig. 11: x-displacement distribution for the bi-material plate subject to a linear body force: (a) ERKPM, (b) RKPM.

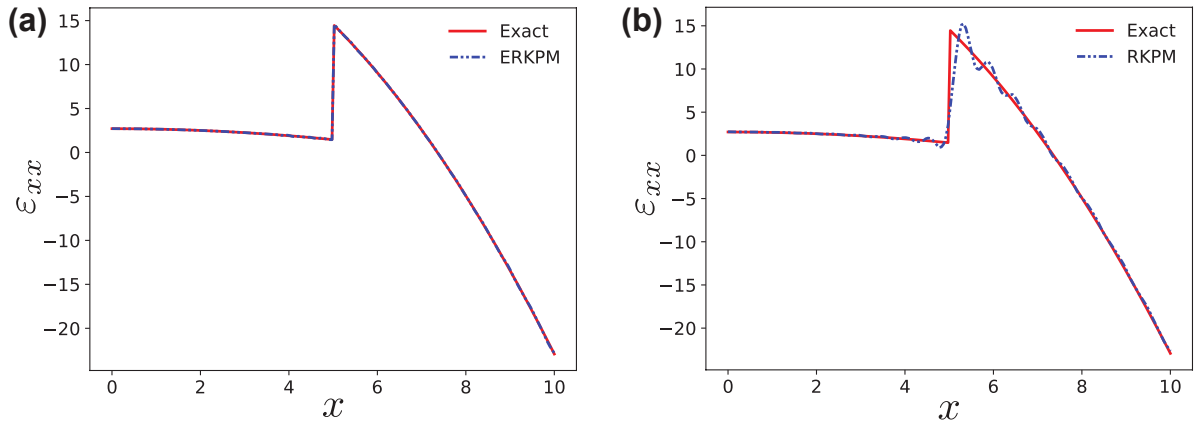

Fig. 12: x-strain distribution for the bi-material plate subject to a linear body force: (a) ERKPM, (b) RKPM.

ERKPM are superior to those of RKPM. Moreover, optimal convergence is achieved by ERKPM, whereas the convergence rates of RKPM are decreased by half as expected in both norms. Figs. 15 and 16 demonstrate the strain and displacement for the non-linear body force. It is clear that the RKPM solution smears the discontinuity in strain in contrast to ERKPM giving very accurate results. Once again, the same problem for a homogeneous plate is considered. In this case, both ERKPM and RKPM yield convergence rates higher than the op-

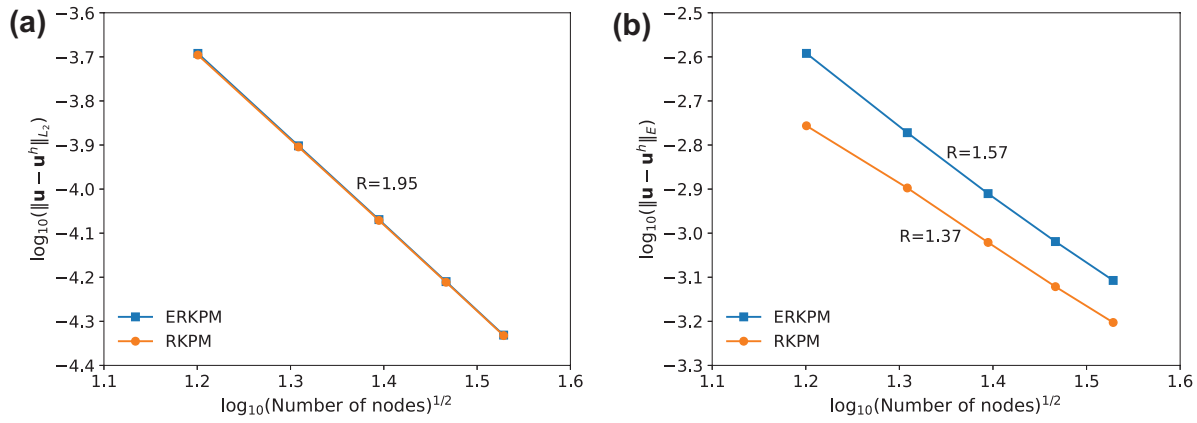

Fig. 13: Convergence results for the homogeneous plate subject to a linear body force: (a) L_2 norm, (b) Energy norm.

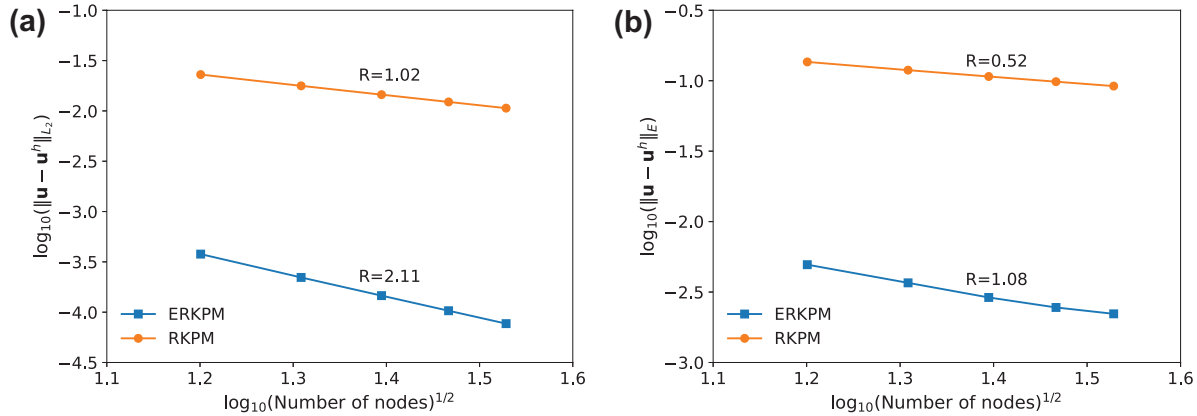

Fig. 14: Convergence results for the bi-material plate subject to a non-linear body force: (a) L_2 norm, (b) Energy norm.

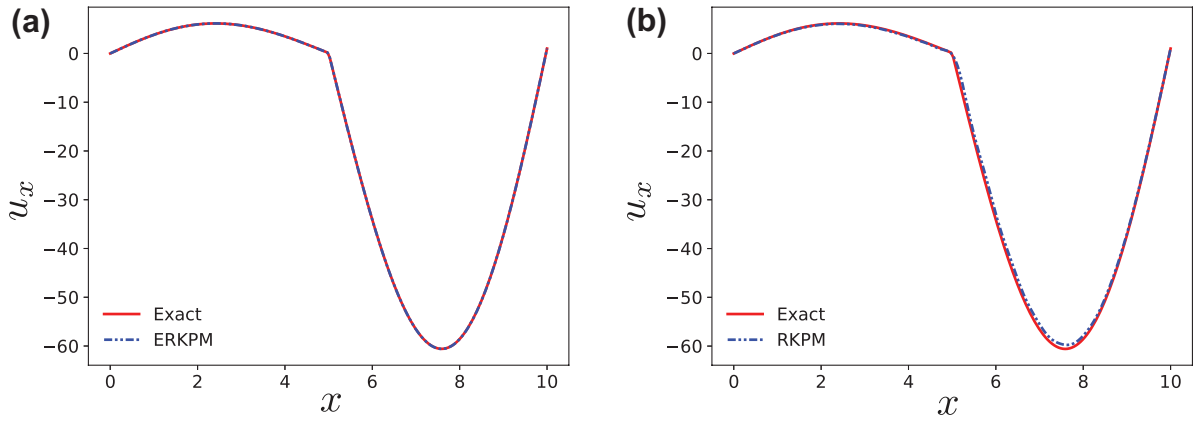

Fig. 15: x-displacement distribution for the bi-material plate subject to a non-linear body force: (a) ERKPM, (b) RKPM.

timal ones in L_2 norm and energy norm as shown in Fig. 17.

6.2 Two-dimensional bi-material problem

In this problem, a circular plate of radius b, whose material constants are $E_1 = 1$ and $\nu_1 = 0.25$, contains a

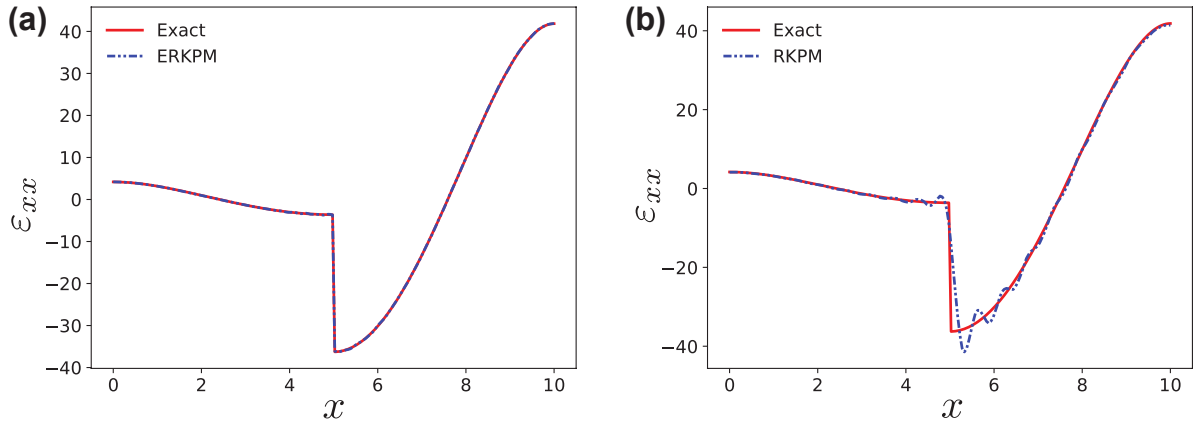

Fig. 16: x-strain distribution for the bi-material plate subject to a non-linear body force: (a) ERKPM, (b) RKPM.

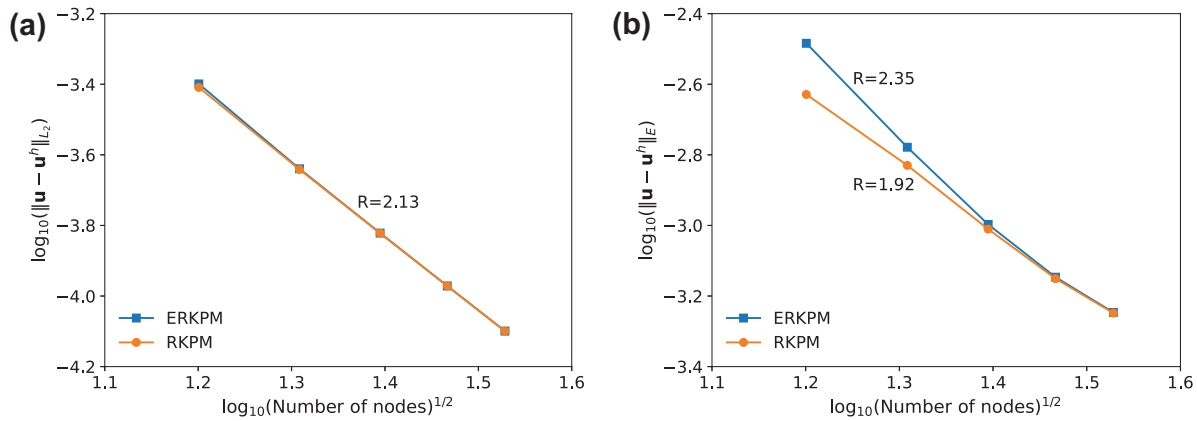

Fig. 17: Convergence results for the homogeneous plate subject to a non-linear body force: (a) L_2 norm, (b) Energy norm.

circular inclusion of radius a, whose material is defined as $E_2 = 10$ and $\nu_2 = 0.3$, as shown in Fig. 18. A linear displacement field is imposed on the outer boundary: $u_r(b,\theta) = r$ and $u_\theta(b,\theta) = 0$. The analytical solution can be found in [37].

In the numerical model, a square domain of size $L \times L$ with $L = 2$ is considered, and the outer radius b and inner radius a are chosen to be 2 and 0.4, respectively. The exact solution is applied on the boundary of the domain as essential BCs. Plane strain condition is assumed. A convergence study is performed by considering various uniform discretization: 30×30, 40×40, 60×60, 80×80, and 100×100. Fig. 19(a) shows a uniform grid for the problem, and its Voronoi tessellation is given in Fig. 19(b). The rates of convergence for each formulation in L_2 norm and energy norm are illustrated in Fig. 20. On the one hand ERKPM achieves a convergence rate of 2.03 in L_2 norm and 1.28 in energy norm, which agrees well with the theoretical ones. On the other hand, RKPM shows poor accuracy and rates of convergence. Fig. 21 displays the oscillating response in radial and hoop strains of RKPM solutions, and ERKPM significantly reduces such oscillatory behaviour at the discontinuity, thus substantially improving the results.

Next we solve this problem for non-uniform discretization, and β_{irr} is chosen to be 0.3 herein. Fig. 22 shows a typical non-uniform discretization and the corresponding Voronoi diagram.

The convergence results in L_2 norm and energy norm are indicated in Figs. 23(a) and 23(b), respectively. The standard RKPM shows a sub-optimal convergence rates, whereas ERKPM still gives an optimal ones for the non-uniform discretization. Moreover, ERKPM solutions for non-uniform discretization have the same order of accuracy as ones for uniform discretization. The radial and hoop strains for an 80×80 grid are illustrated in Fig. 24. There is a good agreement between results predicted by ERKPM and exact solutions, whereas the strains obtained RKPM still wildly oscillate near the interface. It demonstrates that ERKPM works effectively for both regular and irregular distribution.

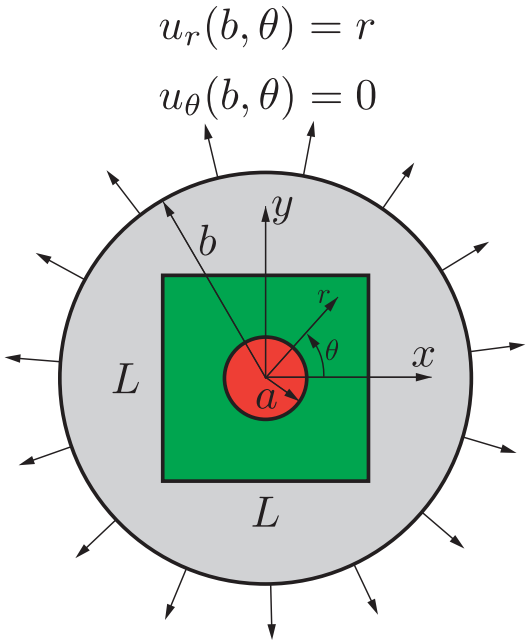

Fig. 18: The two-dimensional bimaterial problem.

6.3 An infinite plate with circular inclusion under far-field tension

In this problem, a far-field uniaxial tension P is applied to an infinite plate containing a circular inclusion with a radius R as shown in Fig. 25. The material properties of the plate are $E_1 = 1$ and $\nu_1 = 0.3$, and those of the inclusion are $E_2 = 10$ and $\nu_2 = 0.3$. The exact solution to this problem can be found in [43].

For the numerical model, we consider a square domain $L \times L$ ($L = 2$) with a circular inclusion of radius $R = 0.4$. Plane stress condition is assumed, and the uniaxial tension $P = 1$ is chosen. The exact displacement is imposed on the boundary of the square domain. In order to study the convergence of each formulation in this problem, we use the same sequences of uniform and non-uniform discretization given in Section 6.2.

For the uniform discretization, Fig. 26 demonstrates the rates of convergence in L_2 norm and energy norm. The ERKPM solutions exhibit optimal convergence rates and outperform the RKPM ones. Specifically, 1.98 and 1.28 are the rates of ERKPM in L_2 and energy norms, and those of RKPM are 0.94 and 0.53, respectively. In addition, not only is the accuracy of the solution improved, but the oscillation is greatly reduced as clearly presented in Fig. 27. Due to the symmetry of the solution, only the strain distributions along positive x are shown.

Regarding the non-uniform discretization, the optimal rates of convergence remain to be obtained by ERKPM as shown in Fig. 28, whereas the reduction by half in rates is observed in the RKPM solutions. The distributions of x-strains along $y = 0$ and shear strains along $y = x$ are given in Figs. 29(a) and 29(b), respectively, for 80×80 discretization. The ERKPM solutions match well with the exact ones, which contrasts with the oscillatory strains predicted by RKPM.

6.4 Multi-inclusion problem

The use of level set method offers an effective tool to model multiple material interfaces with less effort required for model preparation. In this example, we analyze a multi-inclusion unit cell model to demonstrate the effectiveness of the proposed ERKPM. A unit cell contains 10 inclusions with radius $R = 0.1$, whose positions were randomly generated as illustrated in Fig. 30(a). The cell is fixed on one end and displaced a prescribed amount of 0.1 units in the x-direction on the other end. Young's moduli of the cell and inclusions are $E_1 = 1$ and $E_2 = 10$, respectively, while the Poisson's ratio is set to $\nu_1 = \nu_2 = 0.3$ for both of them. An overkill FEM mesh is used as a reference solution, and the elements edges are made to align with the material interfaces. On the other hand, we use a uniform grid with 10,201 nodes for the ERKPM model as depicted in Fig. 30(b). It should be noted that the model does not require nodes on the interfaces.

Figs. 31(a)-(c) show the variations of strains along two cut lines AA' and BB' as plotted in Fig. 30(b). As can be seen from these figures, the RKPM with enrichment can accurately represent multiple jumps in strains due to the presence of several inclusions. The displacements in x- and y-direction are given in Figs. 32 and 33, respectively. It is obvious that due to the effect of inclusions, the displacement field sees a non-symmetric distribution. More interestingly, the interactions between inclusions can be observed in the distribution of x-strains, which results in chain-like patterns as seen in Fig. 34. Additionally, the variations of y-strain and and shear strain are presented in Figs. 35 and 36, respectively. The difference in stiffness between the matrix and the inclusions produces the complex strain fields with highly irregular patterns, and the strain concentration occurs around the interfaces. In comparison with FEM, ERKPM yields similar displacement and strain distributions, which verifies the accuracy of the proposed method.

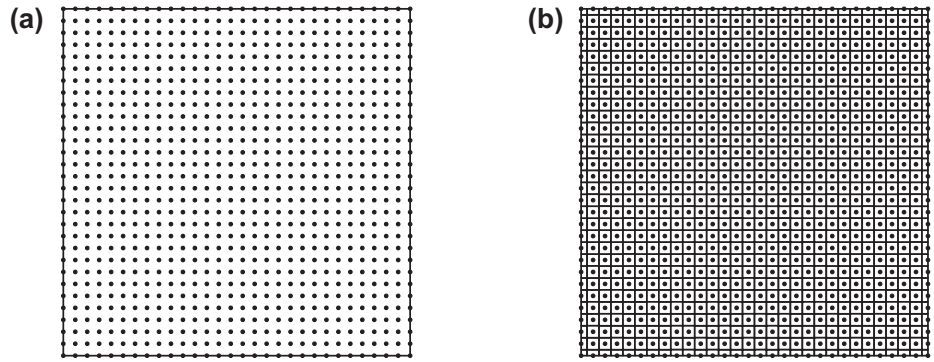

Fig. 19: A uniform 30×30 discretization for the two-dimensional bi-material problem: (a) Nodal distribution, (b) Corresponding Voronoi diagram.

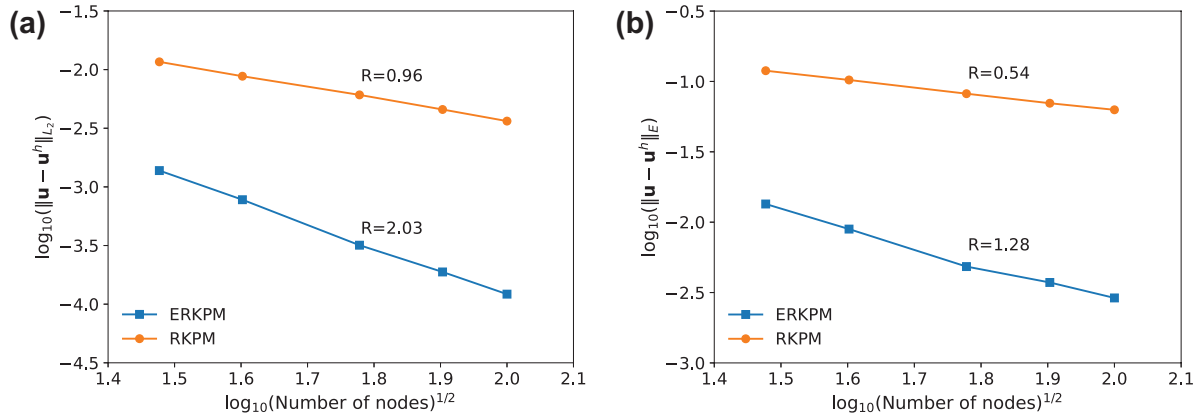

Fig. 20: Convergence results for uniform discretization in the two-dimensional bi-material problem: (a) L_2 norm, (b) Energy norm.

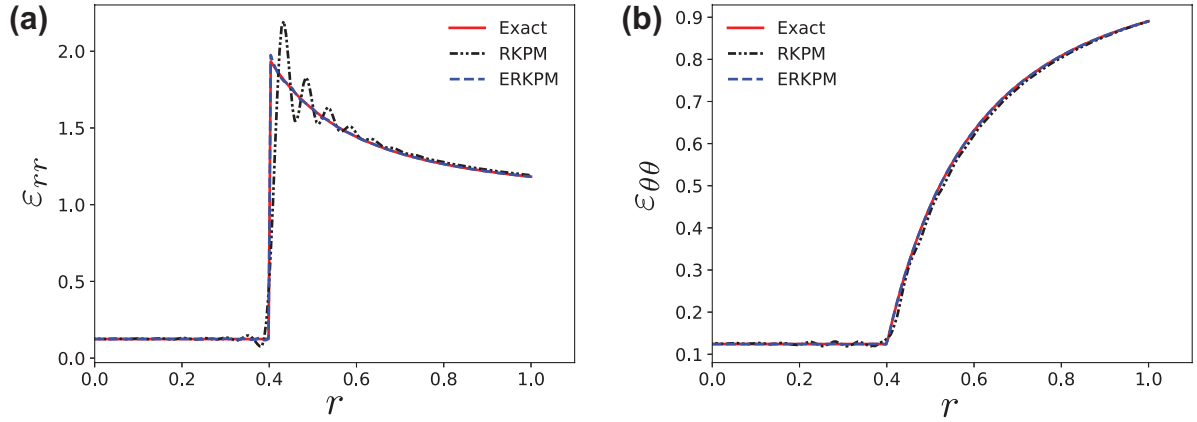

Fig. 21: Strain distribution for uniform discretization in the two-dimensional bi-material problem: (a) Radial strain, (b) Hoop strain.

6.5 Complex interface

In this problem, we aim to investigate the capability of ERKPM to model a more complex-shaped interface. The geometry and BCs are shown in Fig. 37.

The boundary of the inclusion is described by the following function in the polar coordinates:

$$r(\theta) = r_o + A\sin(B\theta), \tag{48}$$

where (r,θ) are the polar coordinates, r_o is the reference radius, B is the number of oscillations, and A denotes

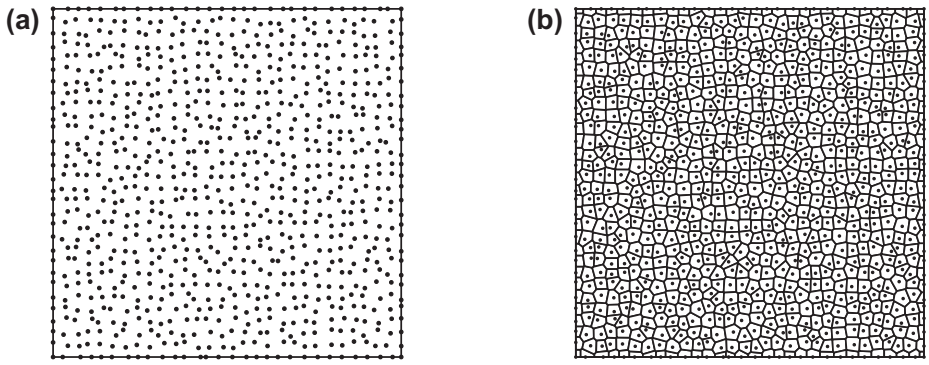

Fig. 22: A non-uniform 30×30 discretization for the two-dimensional bi-material problem: (a) Nodal distribution, (b) Corresponding Voronoi diagram.

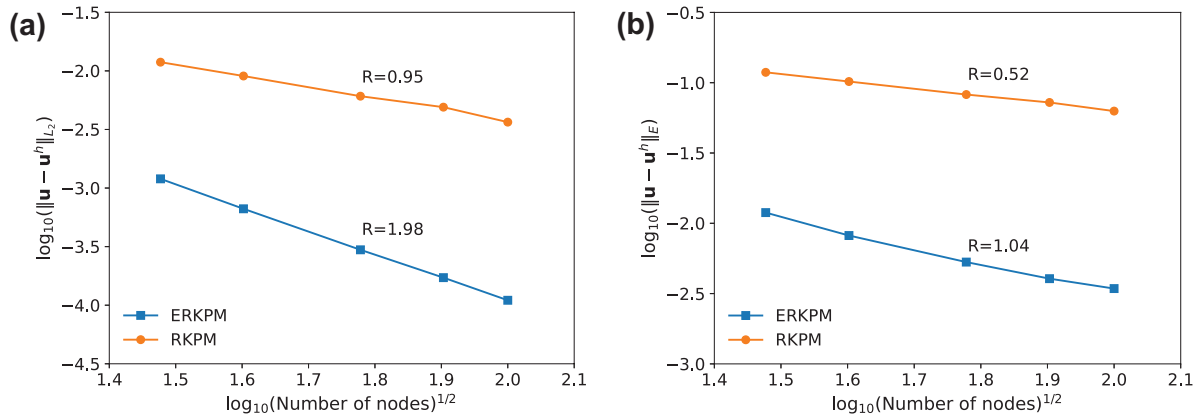

Fig. 23: Convergence results for non-uniform discretization in the two-dimensional bi-material problem: (a) L_2 norm, (b) Energy norm.

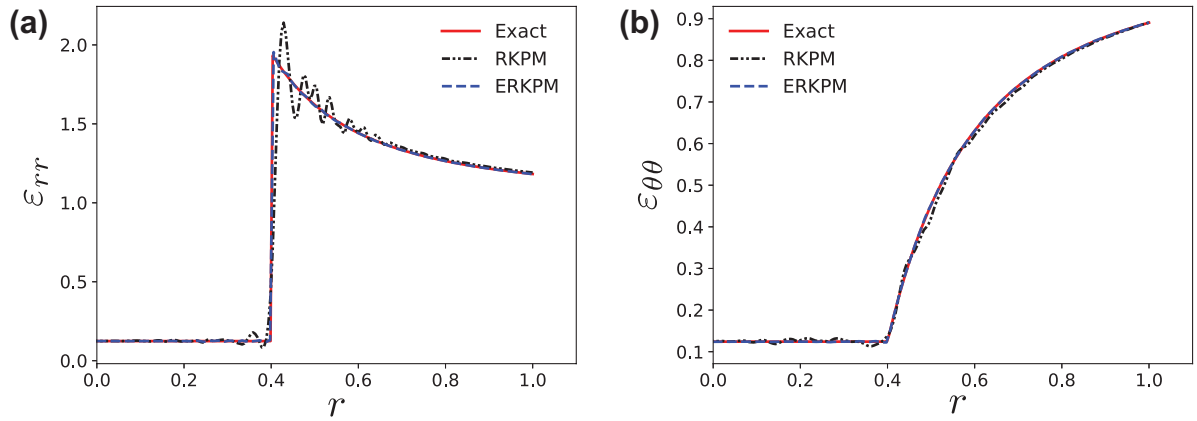

Fig. 24: Strain distribution for non-uniform discretization in the two-dimensional bi-material problem: (a) Radial strain, (b) Hoop strain.

the amplitude of oscillations. In this example, $r_o = 0.5$, $A = 0.125$, and $B = 2$ were chosen.

A conforming FEM model with very fine mesh is considered as a reference solution, whereas an 80×80 uniform discretization is used to solve this problem. We emphasize that for this complicated geometry of the interface, the time devoted to preparing the FEM model is much more than that for the ERKPM model because it is required to align the interface with the element edges. By contrast, the model preparation for ERKPM only takes a fraction of the overall analysis time. Fig. 38 shows a good agreement in the displacement varia-

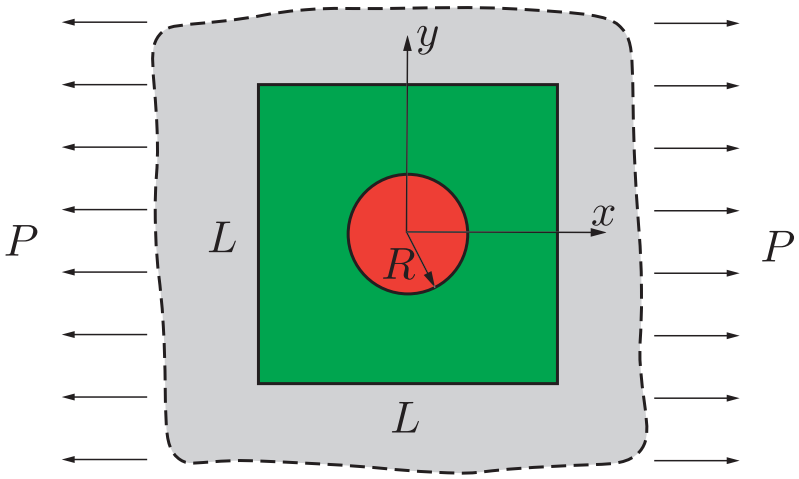

Fig. 25: An infinite inhomogeneous plate under far-field tension.

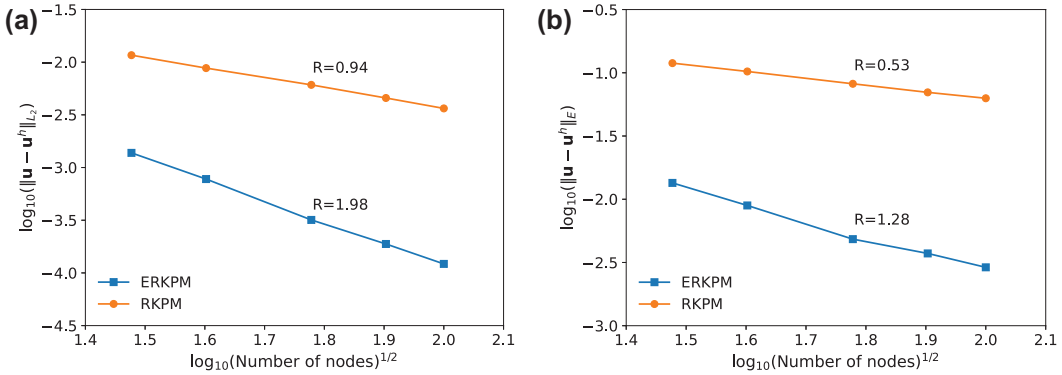

Fig. 26: Convergence results for uniform discretization in the inhomogeneous subject to uniaxial tension: (a) L_2 norm, (b) Energy norm.

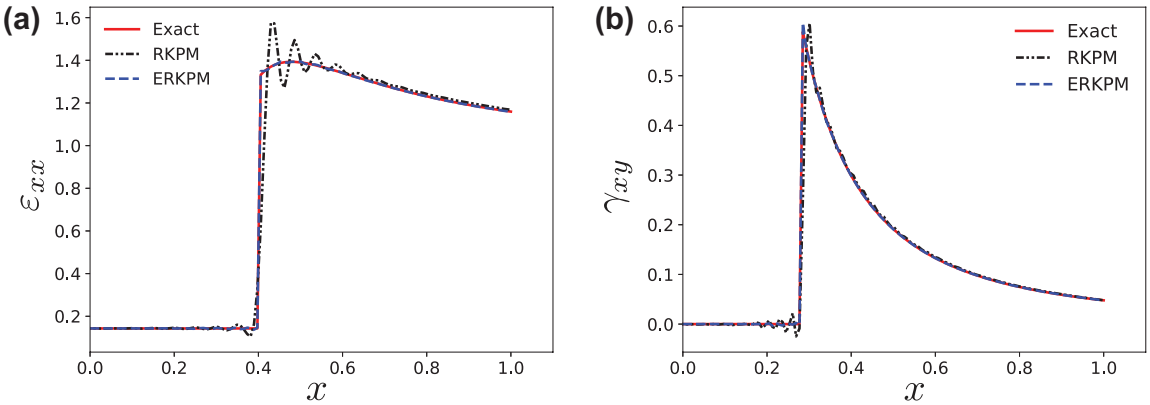

Fig. 27: Strain distribution for uniform discretization in the inhomogeneous subject to uniaxial tension: (a) ε_{xx} along $y = 0$, (b) γ_{xy} along $y = x$.

tion along $x = 0$ between ERKPM and FEM solutions. Moreover, ERKPM captures well the discontinuity in strain as compared to FEM as illustrated in Fig. 39.

The x- and y-displacement fields are illustrated in Fig. 40 and Fig. 41. Because of the incline of the inclusion as well as its geometry, the displacement fields varies in an irregular manner. Figs. 34, 35, and 36 show

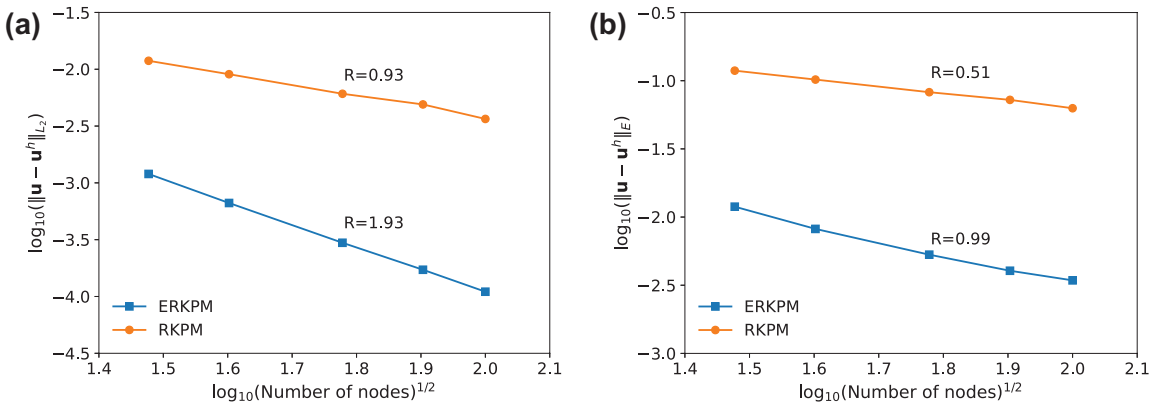

Fig. 28: Convergence results for non-uniform discretization in the inhomogeneous subject to uniaxial tension: (a) L_2 norm, (b) Energy norm.

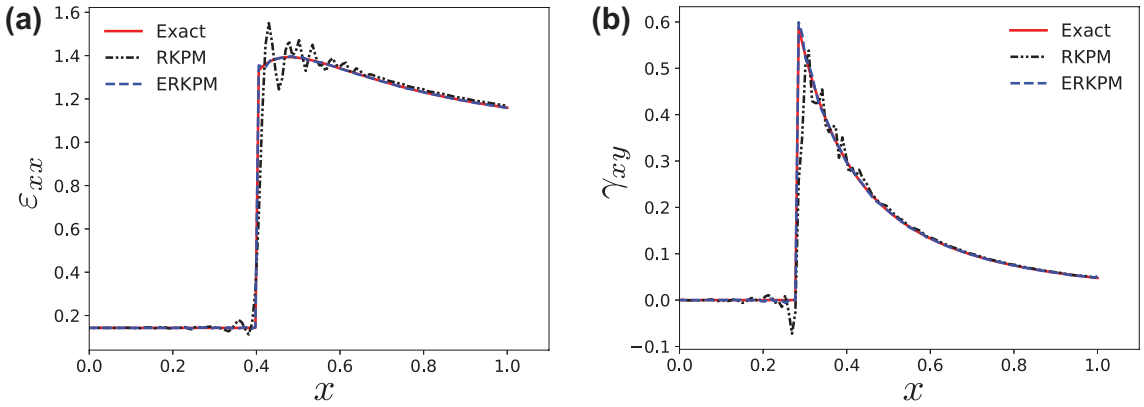

Fig. 29: Strain distribution for non-uniform discretization in the inhomogeneous subject to uniaxial tension: (a) ε_{xx} along $y = 0$, (b) γ_{xy} along $y = x$.

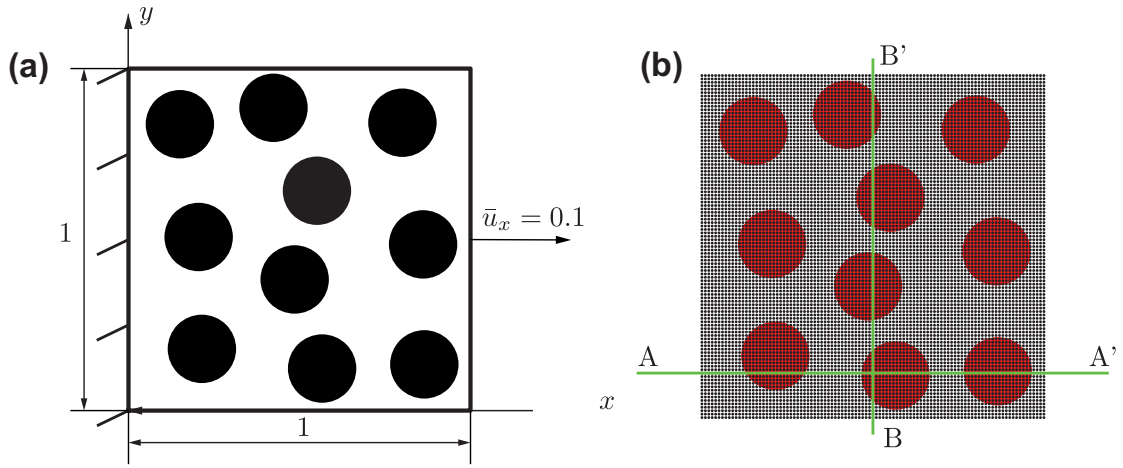

Fig. 30: Setting of the multi-inclusion problem: (a) Geometry and BCs, (b) Uniform discretization of the unit cell.

the distributions of x-, y-, and shear strains, respectively. Discontinuities in strains are well-represented by ERKPM as observed in these figures. Furthermore, a comparison between ERKPM and FEM results shows a reasonable agreement.

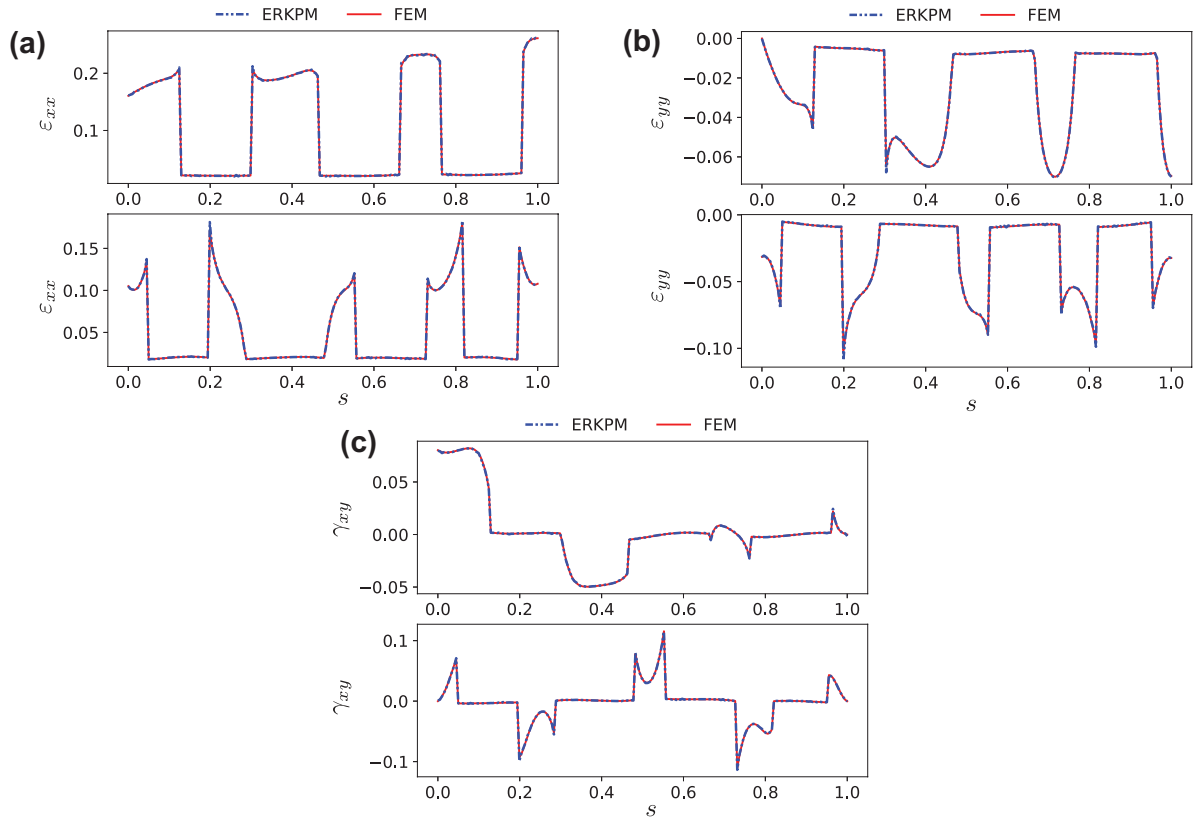

Fig. 31: Distributions of strains along AA' (top) and BB' (bottom) for the multi-inclusion problem: (a) x-strain, (b) y-strain, and (c) shear strain where s denotes x and y coordinates for the top and bottom subfigures, respectively.

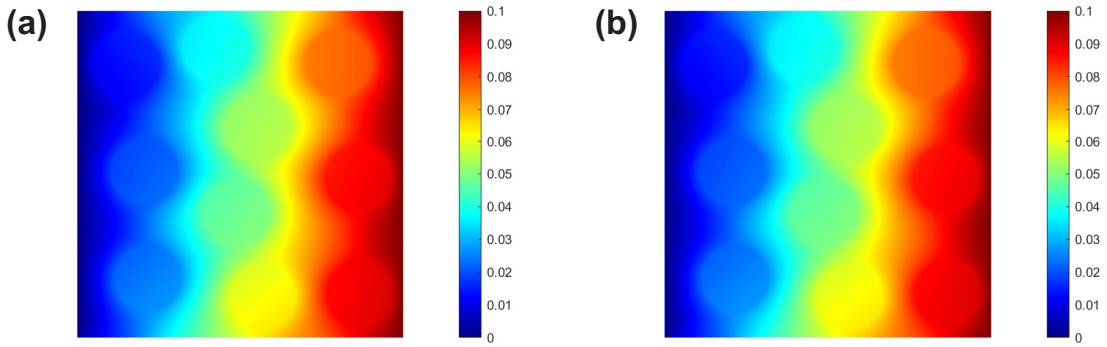

Fig. 32: x-displacement distribution for the multi-inclusion problem: (a) ERKPM, (b) FEM.

7 Conclusions

An enriched RKPM has been described to solve material interface problems in two-dimensional problems. The method is based on adding enriched functions to the approximation space. The level set function is used to implicitly represent the interfaces, and the signed distance function is used to build the local enrichment for material interfaces. Regarding the domain integration, SCNI is used as the main technique. The smoothing operation in SCNI leads to the smoothed strains consisting of the standard part and the enriched one. Furthermore, the variational formulation based on the assumed strain method was revisited to cast the smoothed strains into the weak form. Several numerical examples were given and show the accuracy of the proposed

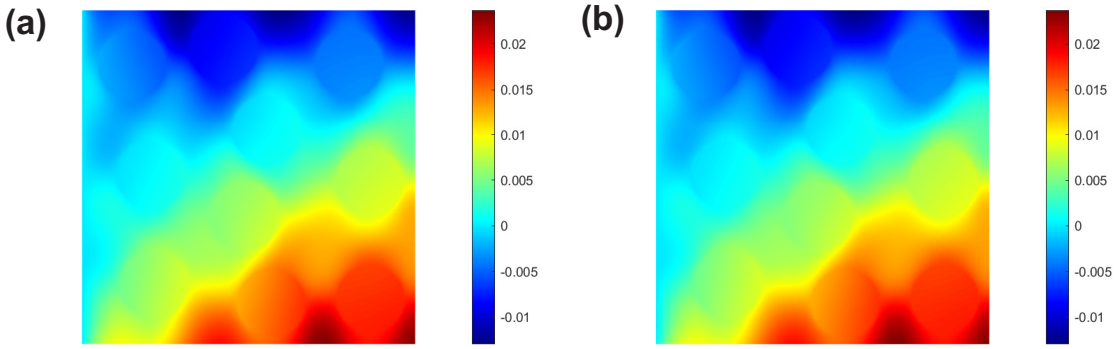

Fig. 33: y-displacement distribution for the multi-inclusion problem: (a) ERKPM, (b) FEM.

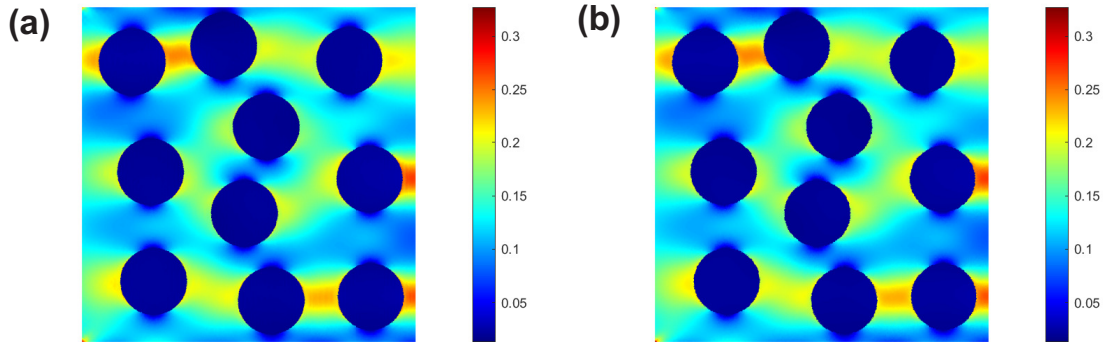

Fig. 34: x-strain distribution for the multi-inclusion problem: (a) ERKPM, (b) FEM.

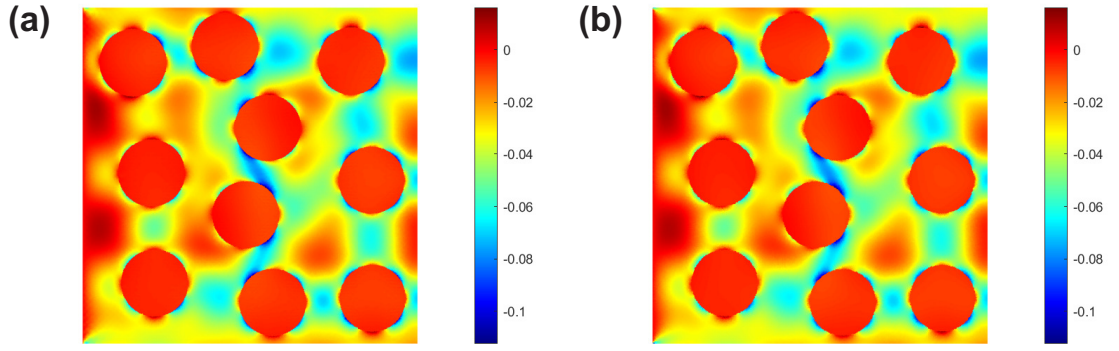

Fig. 35: y-strain distribution for the multi-inclusion problem: (a) ERKPM, (b) FEM.

method. A comparison of the enriched RKPM with either the analytical solutions or FEM demonstrates an excellent agreement and the capability to model problems with complex interface and multiple inclusions. The proposed method effectively reproduces the weak discontinuities and significantly reduces the oscillations

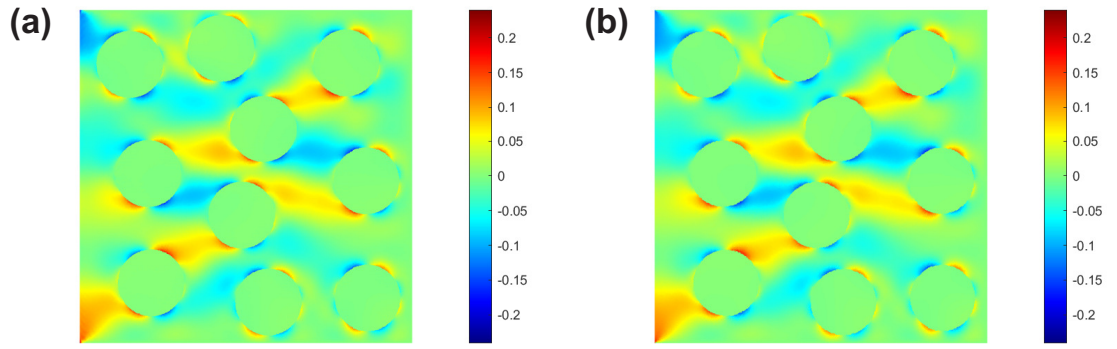

Fig. 36: Shear strain distribution for the multi-inclusion problem: (a) ERKPM, (b) FEM.

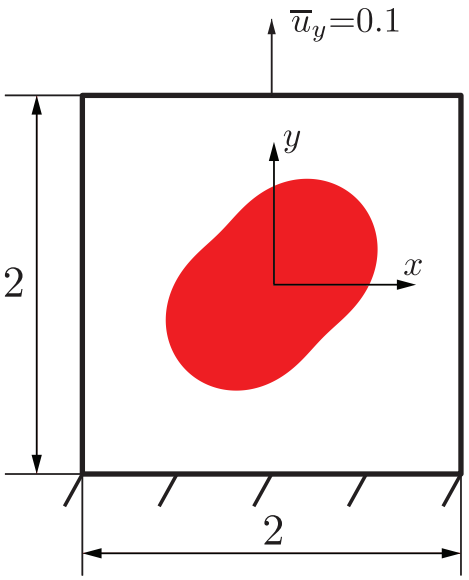

Fig. 37: The geometry and loading of the complex interface problem.

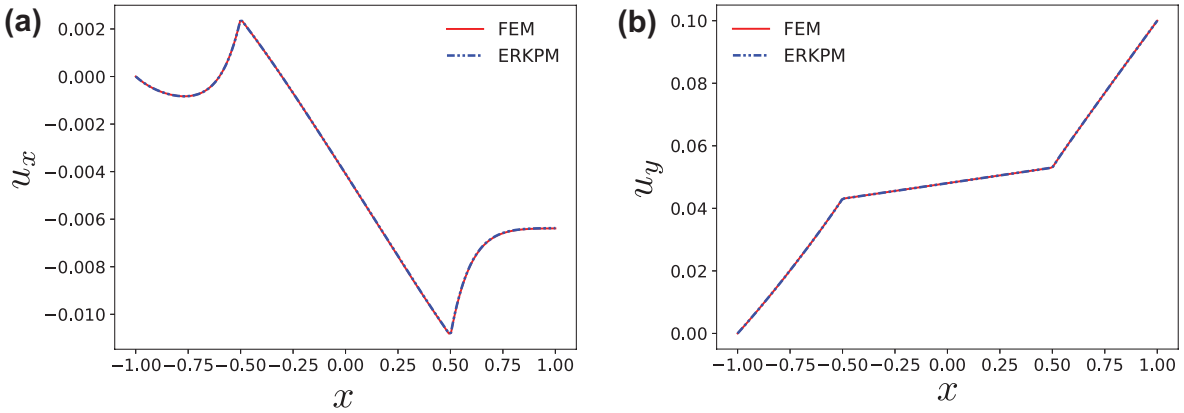

Fig. 38: Displacement distribution along $x = 0$ for the complex interface problem: (a) u_x, (b) u_y.

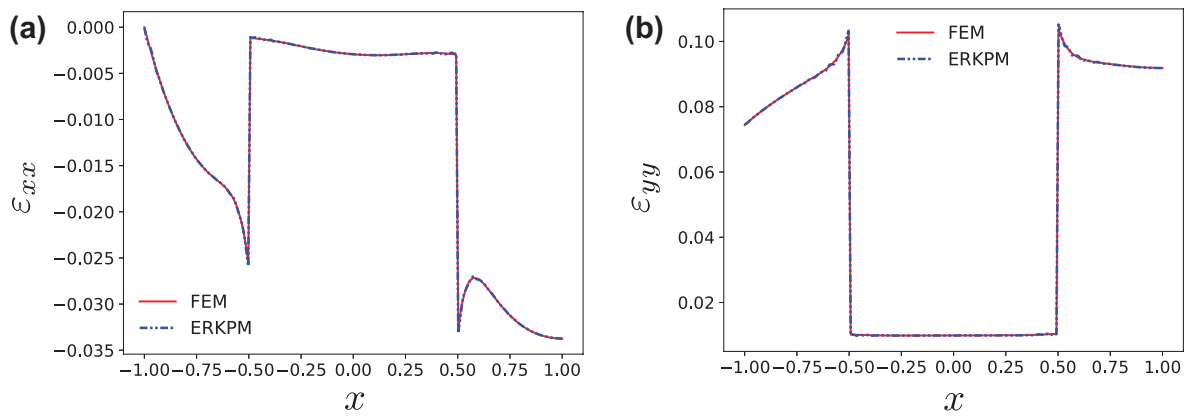

Fig. 39: Strain distribution along $x = 0$ for the complex interface problem: (a) ε_{xx}, (b) ε_{yy}.

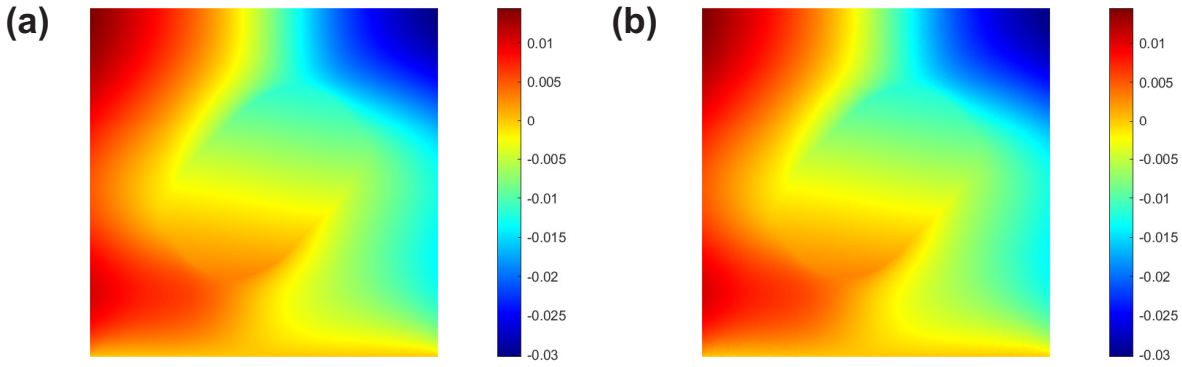

Fig. 40: x-displacement distribution for the complex interface problem: (a) ERKPM, (b) FEM.

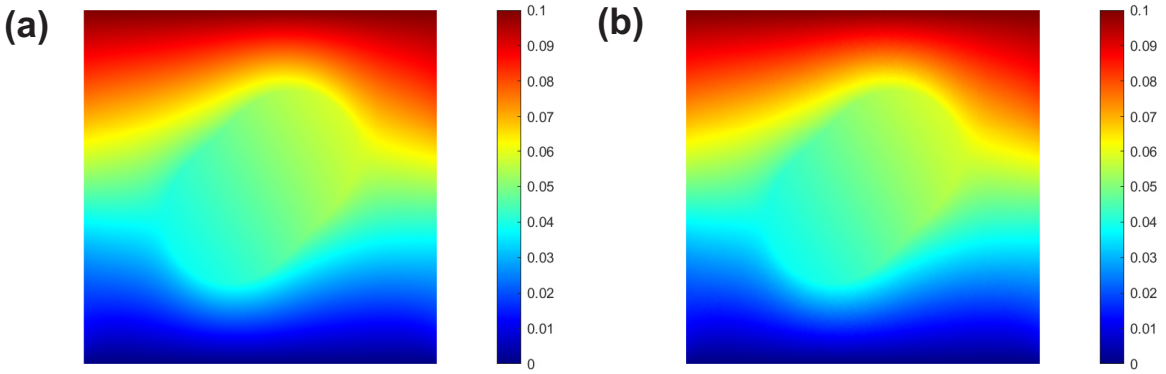

Fig. 41: y-displacement distribution for the complex interface problem: (a) ERKPM, (b) FEM.

as compared with standard RKPM. Moreover, the use of level set method to implicitly represent interface geometries enables less effort for model preparation because interface nodes are not required and the introduction of additional interfaces can be done with little

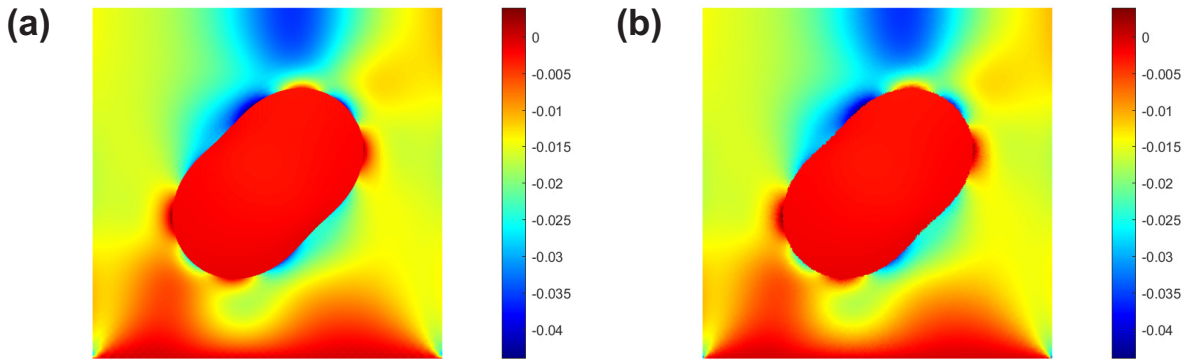

Fig. 42: x-strain distribution for the complex interface problem: (a) ERKPM, (b) FEM.

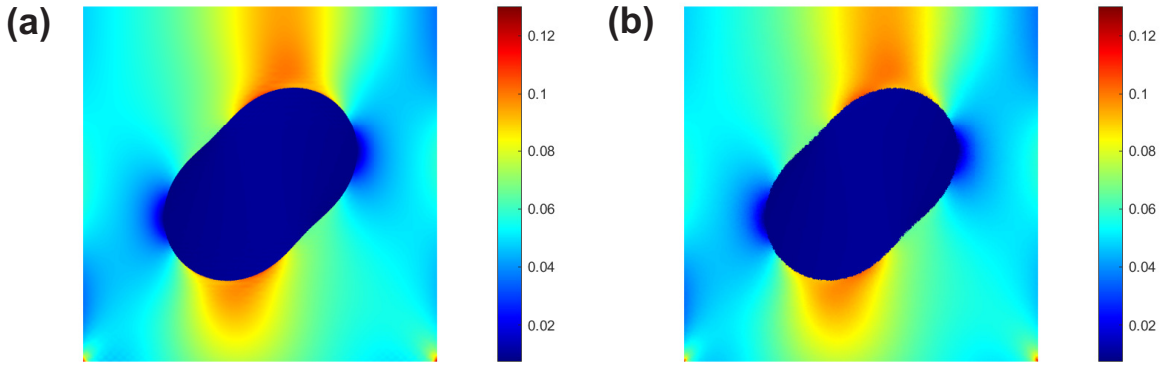

Fig. 43: y-strain distribution for the complex interface problem: (a) ERKPM, (b) FEM.

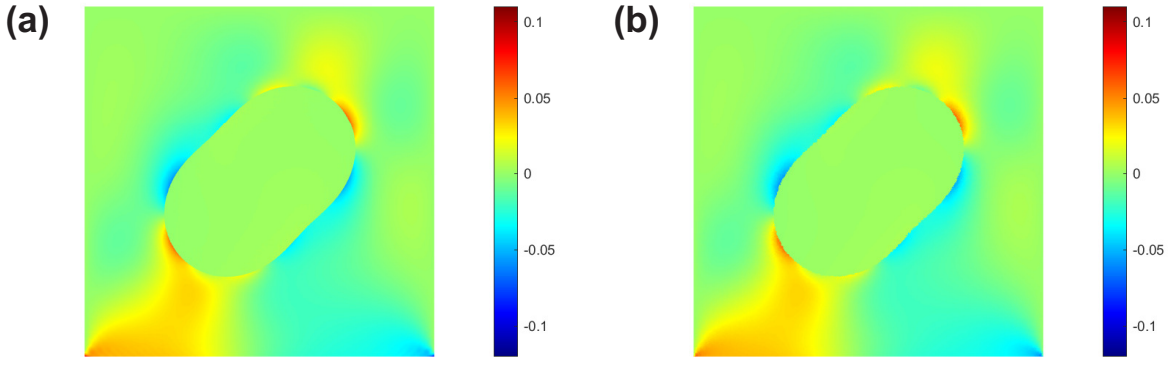

Fig. 44: Shear strain distribution for the complex interface problem: (a) ERKPM, (b) FEM.

extra cost, and this is particularly useful for composite analysis in which multiple interfaces are present.

The enrichment technique for the NI scheme presented in this paper can be extended to deal with strong discontinuity problems such as fracture or interface failure where the strong discontinuities can be described by the sign-enrichment function [44]. Since SCNI demands a construction of the conforming Voronoi cells to perform smoothing operations, it becomes tedious if the Voronoi diagram is required to regenerate. In fact, this is the case for fracture problems in which crack extension changes the topology of smoothing cells, so regeneration of the whole Voronoi cell is a must, adding more expense to the overall computational procedure. As a result, the enrichment method along with the level set method is well-suited to this problem because the need for explicit description of the crack geometry in the model can be circumvented, bypassing conforming cell regeneration. It is worth noting that the requirement of conforming cells can be relaxed by considering stabilized non-conforming nodal integration [45]. However, this method, in many cases, gives unstable solutions and sub-optimal convergence rates, so a correction method [19,20] or a smoothing cell update scheme [46] is required to enhance the solution accuracy of RKPM with non-conforming nodal integration. In addition, it leads to the use of Petrov-Galerkin method, so the discrete system becomes non-symmetric. In the future, the extension of the current work shall be used to tackle this difficulty.

The extension of the proposed method to three-dimensional modeling is possible. Here we briefly mention some challenges that can be expected when doing so. Firstly, the computer implementation of SCNI and enrichment is more involved in the three-dimensional modeling than in the two-dimensional case. Secondly, it is known that using enrichment functions can lead to a higher condition number of the stiffness matrix [44]. The ill-conditioning becomes more severe in three-dimensional modeling, leading to the loss of accuracy of solutions and slow convergence if one uses iterative solvers. Fortunately, this problem was well-studied in the context of extended FEM, so the available techniques can be utilized to handle such difficulties.

8 Acknowledgement

Huy Anh Nguyen is gratefully acknowledged the support of this work by Japanese Government (MEXT) scholarship for his Doctoral Program.

Appendix A: Derivation of the weak form

The basis for the assumed strain method [39,40] is specified by the Hu-Washizu variational principle, which incorporates all field equations from Eqs. (14) and (16)-(18) into the functional and fulfills them in the weak sense. The admissible function spaces for the displacement $\boldsymbol{u}$, stress $\boldsymbol{\sigma}$, assumed strain $\tilde{\boldsymbol{\varepsilon}}$ and Lagrange multiplier $\boldsymbol{\lambda}$ are defined as

$$\mathbb{V} = \{\boldsymbol{u}(\boldsymbol{x}) \in [L^2(\Omega)]^2 : u_{i,j} \in L^2(\Omega),\ i,j = 1,2\}, \tag{A.1a}$$

$$\mathbb{S} = \{\boldsymbol{\sigma}(\boldsymbol{x}) \in [L^2(\Omega)]^{2\times 2} : \boldsymbol{\sigma} = \boldsymbol{\sigma}^T\}, \tag{A.1b}$$

$$\mathbb{E} = \{\boldsymbol{\gamma}(\boldsymbol{x}) \in [L^2(\Omega)]^{2\times 2} : \boldsymbol{\gamma} = \boldsymbol{\gamma}^T\}, \tag{A.1c}$$

$$\Lambda = \{\boldsymbol{\lambda}(\boldsymbol{x}) \in [L^2(\Gamma_u)]^2\}, \tag{A.1d}$$

respectively, and L^2 is the space of square integrable functions. Note that the satisfaction of the essential BCs is not required for elements of $\mathbb{V}$. Let $\Pi_{HW} : \mathbb{V}\times\mathbb{S}\times\mathbb{E}\times\Lambda \to \mathbb{R}$ be the Hu-Washizu functional which is defined as follows,

$$\begin{aligned}
&\Pi_{HW}(\boldsymbol{u},\boldsymbol{\sigma},\tilde{\boldsymbol{\varepsilon}},\boldsymbol{\lambda}) \\
&= \int_\Omega \left\{ \frac{1}{2}\tilde{\boldsymbol{\varepsilon}} : \mathbb{C} : \tilde{\boldsymbol{\varepsilon}} - \boldsymbol{b}\cdot\boldsymbol{u} - \boldsymbol{\sigma} : [\tilde{\boldsymbol{\varepsilon}} - \frac{1}{2}(\nabla\boldsymbol{u} + \nabla\boldsymbol{u}^T)] \right\} dV \\
&- \int_{\Gamma_t} \bar{\boldsymbol{t}}\cdot\boldsymbol{u}\, dS - \int_{\Gamma_u} \boldsymbol{\lambda}\cdot(\boldsymbol{u} - \bar{\boldsymbol{u}})\, dS.
\end{aligned} \tag{A.2}$$

By taking the first variation of the functional Π_{HW} in the standard manner, it yields

$$\begin{aligned}
&\delta\Pi_{HW}(\boldsymbol{u},\boldsymbol{\sigma},\tilde{\boldsymbol{\varepsilon}},\boldsymbol{\lambda}) \\
&= \int_\Omega \delta\tilde{\boldsymbol{\varepsilon}} : (\mathbb{C} : \tilde{\boldsymbol{\varepsilon}} - \boldsymbol{\sigma})\, dV - \int_\Omega \delta\boldsymbol{\sigma} : (\boldsymbol{\varepsilon} - \tilde{\boldsymbol{\varepsilon}})\, dV \\
&+ \int_\Omega \delta\boldsymbol{\varepsilon} : \boldsymbol{\sigma}\, dV - \int_{\Gamma_u} \delta\boldsymbol{\lambda}\cdot(\boldsymbol{u} - \bar{\boldsymbol{u}})\, dS \\
&- \int_{\Gamma_u} \delta\boldsymbol{u}\cdot\boldsymbol{\lambda}\, dS - \int_\Omega \delta\boldsymbol{u}\cdot\boldsymbol{b}\, dV - \int_{\Gamma_t} \delta\boldsymbol{u}\cdot\bar{\boldsymbol{t}}\, dS,
\end{aligned} \tag{A.3}$$

where $\delta\boldsymbol{u} \in \mathbb{V}$, $\delta\boldsymbol{\sigma} \in \mathbb{S}$, $\delta\tilde{\boldsymbol{\varepsilon}} \in \mathbb{E}$, and $\delta\boldsymbol{\lambda} \in \Lambda$ are the admissible variations of the displacement $\boldsymbol{u}$, stress $\boldsymbol{\sigma}$, assumed strain $\tilde{\boldsymbol{\varepsilon}}$ and Lagrange multiplier $\boldsymbol{\lambda}$, respectively, and $\delta\boldsymbol{\varepsilon} = (\nabla\delta\boldsymbol{u} + \nabla\delta\boldsymbol{u}^T)/2$. Then, we pose the following variational problem:

Find $(\boldsymbol{u},\boldsymbol{\sigma},\tilde{\boldsymbol{\varepsilon}},\boldsymbol{\lambda}) \in \mathbb{V}\times\mathbb{S}\times\mathbb{E}\times\Lambda$ such that,

$$\int_\Omega \delta\tilde{\boldsymbol{\varepsilon}} : (\mathbb{C} : \tilde{\boldsymbol{\varepsilon}} - \boldsymbol{\sigma})\, dV = 0, \tag{A.4a}$$

$$\int_\Omega \delta\boldsymbol{\sigma} : (\boldsymbol{\varepsilon} - \tilde{\boldsymbol{\varepsilon}})\, dV = 0, \tag{A.4b}$$

$$\begin{aligned}
&\int_\Omega \delta\boldsymbol{\varepsilon} : \boldsymbol{\sigma}\, dV - \int_\Omega \delta\boldsymbol{u}\cdot\boldsymbol{b}\, dV - \int_{\Gamma_t} \delta\boldsymbol{u}\cdot\bar{\boldsymbol{t}}\, dS \\
&\qquad - \int_{\Gamma_u} \delta\boldsymbol{u}\cdot\boldsymbol{\lambda}\, dS = 0,
\end{aligned} \tag{A.4c}$$

$$\int_{\Gamma_u} \delta\boldsymbol{\lambda}\cdot(\boldsymbol{u} - \bar{\boldsymbol{u}})\, dS = 0, \tag{A.4d}$$

for all $(\delta\boldsymbol{u},\delta\boldsymbol{\sigma},\delta\tilde{\boldsymbol{\varepsilon}},\delta\boldsymbol{\lambda}) \in \mathbb{V}\times\mathbb{S}\times\mathbb{E}\times\Lambda$. By the standard argument, it can be shown that Eqs. (A.4a)-(A.4d) are equivalent to Eqs. (14) and (16)-(18). Furthermore, carrying out integration by part on the first term of Eq. (A.4c) gives,

$$\begin{aligned}
&\int_\Omega \delta\boldsymbol{u}\cdot(\nabla\cdot\boldsymbol{\sigma} - \boldsymbol{b})\, dV - \int_{\Gamma_t} \delta\boldsymbol{u}\cdot(\boldsymbol{\sigma}\boldsymbol{n} - \bar{\boldsymbol{t}})\, dS \\
&- \int_{\Gamma_u} \delta\boldsymbol{u}\cdot(\boldsymbol{\sigma}\boldsymbol{n} - \boldsymbol{\lambda})\, dS = 0.
\end{aligned} \tag{A.5}$$

From Eq. (A.5), it illustrates that the physical significance of the Lagrangian term $\boldsymbol{\lambda}$ is the traction on the essential boundary Γ_u. Hence, $\boldsymbol{\lambda}$ can be replaced by $\boldsymbol{\sigma}\cdot\boldsymbol{n}$.

Let $\mathbb{V}^h$, $\mathbb{S}^h$, $\mathbb{E}^h$, and Λ^h be the finite-dimensional subspaces of $\mathbb{V}$, $\mathbb{S}$, $\mathbb{E}$, and Λ, respectively, i.e., $\mathbb{V}^h \subseteq \mathbb{V}$, $\mathbb{S}^h \subseteq \mathbb{S}$, $\mathbb{E}^h \subseteq \mathbb{E}$, and $\Lambda^h \subseteq \Lambda$. Additionally, let $\boldsymbol{\varepsilon}^h := \boldsymbol{\varepsilon}(\boldsymbol{u}^h)$. We have the discrete version of the foregoing variational problem: Find $(\boldsymbol{u}^h, \boldsymbol{\sigma}^h, \tilde{\boldsymbol{\varepsilon}}^h, \boldsymbol{\lambda}^h) \in \mathbb{V}^h \times \mathbb{S}^h \times \mathbb{E}^h \times \Lambda^h$ such that,

$$\int_\Omega \delta\tilde{\boldsymbol{\varepsilon}}^h : (\mathbb{C} : \tilde{\boldsymbol{\varepsilon}}^h - \boldsymbol{\sigma}^h)\, dV = 0, \tag{A.6a}$$

$$\int_\Omega \delta\boldsymbol{\sigma}^h : (\boldsymbol{\varepsilon}^h - \tilde{\boldsymbol{\varepsilon}}^h)\, dV = 0, \tag{A.6b}$$

$$\int_\Omega \delta\boldsymbol{\varepsilon}^h : \boldsymbol{\sigma}^h\, dV - \int_\Omega \delta\boldsymbol{u}^h \cdot \boldsymbol{b}\, dV - \int_{\Gamma_t} \delta\boldsymbol{u}^h \cdot \bar{\boldsymbol{t}}\, dS - \int_{\Gamma_u} \delta\boldsymbol{u}^h \cdot \boldsymbol{\lambda}^h\, dS = 0, \tag{A.6c}$$

$$\int_{\Gamma_u} \delta\boldsymbol{\lambda}^h \cdot (\boldsymbol{u}^h - \bar{\boldsymbol{u}})\, dS = 0, \tag{A.6d}$$

for all $(\delta\boldsymbol{u}^h, \delta\boldsymbol{\sigma}^h, \delta\tilde{\boldsymbol{\varepsilon}}^h, \delta\boldsymbol{\lambda}^h) \in \mathbb{V}^h \times \mathbb{S}^h \times \mathbb{E}^h \times \Lambda^h$.

The key step in deriving an assumed strain method is to construct an assumed strain field to satisfy the **orthogonality condition** [39,40].

$$\int_\Omega \boldsymbol{\tau} : \boldsymbol{\gamma}\, dV = 0, \text{ for all } \boldsymbol{\tau} \in \mathbb{S}^h \text{ and } \boldsymbol{\gamma} \in \mathbb{E}^h_e, \tag{A.7}$$

where $\mathbb{E}^h_e = \{\boldsymbol{\gamma} \in [L^2(\Omega)]^{2\times 2} : \boldsymbol{\gamma} = \boldsymbol{\varepsilon}^h - \tilde{\boldsymbol{\varepsilon}}^h\}$. The orthogonality condition states that the space of admissible stress field is orthogonal to the space of the enhanced strain field, i.e., the difference between the compatible strain field and the assumed strain field. Furthermore, the fulfillment of the orthogonality condition allows expressing Eq. (A.6c) in terms of the assumed strains only by observing that

$$\begin{aligned}
&\int_\Omega \delta\boldsymbol{\varepsilon}^h : \boldsymbol{\sigma}^h\, dV \\
&= \int_\Omega (\delta\boldsymbol{\varepsilon}^h - \delta\tilde{\boldsymbol{\varepsilon}}^h) : \boldsymbol{\sigma}^h\, dV + \int_\Omega \delta\tilde{\boldsymbol{\varepsilon}}^h : \boldsymbol{\sigma}^h\, dV \\
&= \int_\Omega \delta\tilde{\boldsymbol{\varepsilon}}^h : \boldsymbol{\sigma}^h\, dV,
\end{aligned}$$

and by (A.6a),

$$\int_\Omega \delta\boldsymbol{\varepsilon}^h : \boldsymbol{\sigma}^h\, dV = \int_\Omega \delta\tilde{\boldsymbol{\varepsilon}}^h : \mathbb{C} : \tilde{\boldsymbol{\varepsilon}}^h\, dV. \tag{A.8}$$

Now, we consider whether or not the variational problem Eq. (A.6) with the assumed strain given a priori in Eq. (13) is variationally consistent. Firstly, assume that the discrete stresses $\boldsymbol{\sigma}^h$ are computed by the relation

$$\boldsymbol{\sigma}^h = \mathbb{C} : \tilde{\boldsymbol{\varepsilon}}^h. \tag{A.9}$$

Consequently, Eq. (A.6a) is fulfilled exactly. Next, we need to verify the orthogonality condition Eq. (A.7) satisfied by the given assumed strain.

Recall that the problem domain Ω is decomposed into conforming and non-overlapping cells $\{\Omega_L\}_{L=1}^{NP}$, and each cell Ω_L is further subdivided into several conforming subcells $\{\Omega_L^K\}_{K=1}^{NSC}$ where NSC is the number of subcells contained in Ω_L. The discrete counterpart of the assumed strain presented in Eq. (13) is given by

$$\tilde{\boldsymbol{\varepsilon}}^h(\boldsymbol{x}_L^K) = \frac{1}{A_L^K}\int_{\Omega_L^K} \boldsymbol{\varepsilon}(\boldsymbol{u}^h)\, dV. \tag{A.10}$$

Remark:

- If a cell Ω_L is not subdivided, the discrete form of Eq. (15) is used instead.
- The assumed strain is defined to be constant over each subcell Ω_L^K or a cell Ω_L if it is not subdivided.
- The assumed strains $\tilde{\boldsymbol{\varepsilon}}(\boldsymbol{u}^h)$ only depend on the discrete displacement field $\boldsymbol{u}^h$.

Now, we prove that the orthogonality condition Eq. (A.7) is satisfied for the given assumed strain. By assuming the material properties are constant in Ω_L^K and using the fact that $\tilde{\boldsymbol{\varepsilon}}^h(\boldsymbol{x}_L^K)$ is constant in Ω_L^K,

$$\begin{aligned}
&\int_\Omega \boldsymbol{\sigma}^h : \boldsymbol{\varepsilon}^h\, dV \\
&= \int_\Omega \tilde{\boldsymbol{\varepsilon}}^h : \mathbb{C} : \boldsymbol{\varepsilon}^h\, dV \\
&= \sum_{L=1}^{NP} \int_{\Omega_L} \tilde{\boldsymbol{\varepsilon}}^h : \mathbb{C} : \boldsymbol{\varepsilon}^h\, dV \\
&= \sum_{L=1}^{NP}\sum_{K=1}^{NSC} \int_{\Omega_L^K} \tilde{\boldsymbol{\varepsilon}}^h(\boldsymbol{x}_L^K) : \mathbb{C} : \boldsymbol{\varepsilon}(\boldsymbol{u}^h)\, dV \\
&= \sum_{L=1}^{NP}\sum_{K=1}^{NSC} \tilde{\boldsymbol{\varepsilon}}^h(\boldsymbol{x}_L^K) : \mathbb{C} : \int_{\Omega_L^K} \boldsymbol{\varepsilon}(\boldsymbol{u}^h)\, dV \\
&= \sum_{L=1}^{NP}\sum_{K=1}^{NSC} \tilde{\boldsymbol{\varepsilon}}^h(\boldsymbol{x}_L^K) : \mathbb{C} : \tilde{\boldsymbol{\varepsilon}}^h(\boldsymbol{x}_L^K)\, A_L^K \\
&= \sum_{L=1}^{NP}\sum_{K=1}^{NSC} \int_{\Omega_L^K} \tilde{\boldsymbol{\varepsilon}}^h(\boldsymbol{x}_L^K) : \mathbb{C} : \tilde{\boldsymbol{\varepsilon}}^h(\boldsymbol{x}_L^K)\, dV \\
&= \int_\Omega \tilde{\boldsymbol{\varepsilon}}^h : \mathbb{C} : \tilde{\boldsymbol{\varepsilon}}^h\, dV \\
&= \int_\Omega \boldsymbol{\sigma}^h : \tilde{\boldsymbol{\varepsilon}}^h\, dV,
\end{aligned}$$

where Eq. (A.10) is used in the fifth equality.

Therefore, the orthogonality condition is achieved with the use of the given assumed strain. Finally, using the fact that $\boldsymbol{\lambda}^h = \boldsymbol{\sigma}^h\boldsymbol{n}$ on Γ_u and Eq. (A.8) allows rewriting Eq. (A.6) into a single equation

$$\begin{aligned}
&\int_\Omega \delta\tilde{\boldsymbol{\varepsilon}}^h : \mathbb{C} : \tilde{\boldsymbol{\varepsilon}}^h\, dV - \int_\Omega \delta\boldsymbol{u}^h \cdot \boldsymbol{b}\, dV - \int_{\Gamma_t} \delta\boldsymbol{u}^h \cdot \bar{\boldsymbol{t}}\, dS \\
&- \int_{\Gamma_u} \delta\boldsymbol{u}^h \cdot \boldsymbol{t}^h\, dS - \int_{\Gamma_u} \delta\boldsymbol{t}^h \cdot (\boldsymbol{u}^h - \bar{\boldsymbol{u}})\, dS = 0,
\end{aligned} \tag{A.11}$$

where $\boldsymbol{t}^h = \boldsymbol{\sigma}^h\boldsymbol{n} = (\mathbb{C} : \tilde{\boldsymbol{\varepsilon}}^h)\cdot\boldsymbol{n}$. To improve the coercivity of the variational formulation in Eq. (A.11), adding a penalty-like term to it yields [47]

$$\begin{aligned}
&\int_\Omega \delta\tilde{\boldsymbol{\varepsilon}}^h : \mathbb{C} : \tilde{\boldsymbol{\varepsilon}}^h\, dV - \int_{\Gamma_u} \delta\boldsymbol{u}^h \cdot \boldsymbol{t}^h\, dS \\
&- \int_{\Gamma_u} \delta\boldsymbol{t}^h \cdot (\boldsymbol{u}^h - \bar{\boldsymbol{u}})\, dS + \alpha\int_{\Gamma_u} \delta\boldsymbol{u}^h \cdot (\boldsymbol{u}^h - \bar{\boldsymbol{u}})\, dS \\
&= \int_\Omega \delta\boldsymbol{u}^h \cdot \boldsymbol{b}\, dV + \int_{\Gamma_t} \delta\boldsymbol{u}^h \cdot \bar{\boldsymbol{t}}\, dS.
\end{aligned} \tag{A.12}$$

References

1. Belytschko T, Lu YY, Gu L (1994) Element-free Galerkin methods. Int J Numer Methods Eng 37:229–256
2. Liu WK, Jun S, Zhang YF (1995) Reproducing kernel particle methods. Int J Numer Methods Fluids 20:1081–1106

3. Duarte CA, Oden JT (1996) H-p clouds—an h-p meshless method. Numer Methods Partial Differ Equ 12:673–705
4. Atluri SN, Zhu T (1998) A new Meshless Local Petrov-Galerkin (MLPG) approach in computational mechanics. Comput Mech 22:117–127
5. De S, Bathe KJ (2000) The method of finite spheres. Comput Mech 25:329–345
6. Arroyo M, Ortiz M (2006) Local maximum-entropy approximation schemes: a seamless bridge between finite elements and meshfree methods. Int J Numer Methods Eng 65:2167–2202
7. Chen J-S, Pan C, Wu C-T (1997) Large deformation analysis of rubber based on a reproducing kernel particle method. Comput Mech 19:211–227
8. Rabczuk T, Belytschko T (2007) A three-dimensional large deformation meshfree method for arbitrary evolving cracks. Comput Methods Appl Mech Eng 196:2777–2799
9. Belytschko T, Lu YY, Gu L (1995) Crack propagation by element-free Galerkin methods. Eng Fract Mech 51:295–315
10. Belytschko T, Tabbara M (1996) Dynamic Fracture Using Element-Free Galerkin Methods. Int J Numer Methods Eng 39:923–938
11. Rabczuk T, Bordas S, Zi G (2007) A three-dimensional meshfree method for continuous multiple-crack initiation, propagation and junction in statics and dynamics. Comput Mech 40:473–495
12. Tanaka S, Suzuki H, Sadamoto S, Sannomaru S, Yu T, Bui TQ (2016) J-integral evaluation for 2D mixed-mode crack problems employing a meshfree stabilized conforming nodal integration method. Comput Mech 58:185–198
13. Sadamoto S, Ozdemir M, Tanaka S, Taniguchi K, Yu TT, Bui TQ (2017) An effective meshfree reproducing kernel method for buckling analysis of cylindrical shells with and without cutouts. Comput Mech 59:919–932
14. Wang D, Chen J-S (2008) A Hermite reproducing kernel approximation for thin-plate analysis with sub-domain stabilized conforming integration. Int J Numer Methods Eng 74:368–390
15. Wang D, Lin Z (2011) Dispersion and transient analyses of Hermite reproducing kernel Galerkin meshfree method with sub-domain stabilized conforming integration for thin beam and plate structures. Comput Mech 48:47–63
16. Dolbow J, Belytschko T (1999) Numerical integration of the Galerkin weak form in meshfree methods. Comput Mech 23:219–230
17. Beissel S, Belytschko T (1996) Nodal integration of the element-free Galerkin method. Comput Methods Appl Mech Eng 139:49–74
18. Chen J-S, Wu C-T, Yoon S, You Y (2001) A stabilized conforming nodal integration for Galerkin mesh-free methods. Int J Numer Methods Eng 50:435–466
19. Chen J-S, Hillman M, Rüter M (2013) An arbitrary order variationally consistent integration for Galerkin meshfree methods. Int J Numer Methods Eng 95:387–418
20. Hillman M, Chen J-S (2016) An accelerated, convergent, and stable nodal integration in Galerkin meshfree methods for linear and nonlinear mechanics. Int J Numer Methods Eng 107:603–630
21. Huang T-H, Wei H, Chen J-S, Hillman M (2020) RKPM2D: an open-source implementation of nodally integrated reproducing kernel particle method for solving partial differential equations. Comp Part Mech 7:393–433
22. Dyka CT, Randles PW, Ingel RP (1997) Stress points for tension instability in SPH. Int J Numer Methods Eng 40:2325–2341
23. Bonet J, Kulasegaram S (2000) Correction and stabilization of smooth particle hydrodynamics methods with applications in metal forming simulations. Int J Numer Methods Eng 47:1189–1214
24. Puso MA, Chen JS, Zywicz E, Elmer W (2008) Meshfree and finite element nodal integration methods. Int J Numer Methods Eng 74:416–446
25. Wu CT, Koishi M, Hu W (2015) A displacement smoothing induced strain gradient stabilization for the meshfree Galerkin nodal integration method. Comput Mech 56:19–37
26. Wu CT, Wu Y, Lyu D, Pan X, Hu W (2020) The momentum-consistent smoothed particle Galerkin (MC-SPG) method for simulating the extreme thread forming in the flow drill screw-driving process. Comp Part Mech 7:177–191
27. Cordes LW, Moran B (1996) Treatment of material discontinuity in the Element-Free Galerkin method. Comput Methods Appl Mech Eng 139:75–89
28. Krongauz Y, Belytschko T (1998) EFG approximation with discontinuous derivatives. Int J Numer Methods Eng 41:1215–1233
29. Wang D, Chen J-S, Sun L (2003) Homogenization of magnetostrictive particle-filled elastomers using an interface-enriched reproducing kernel particle method. Finite Elem Anal Des 39:765–782
30. Liu CW, Taciroglu E (2006) Enriched reproducing kernel particle method for piezoelectric structures with arbitrary interfaces. Int J Numer Methods Eng 67:1565–1586
31. Joyot P, Trunzler J, Chinesta F (2005) Enriched reproducing kernel approximation: reproducing functions with discontinuous derivatives. Lect Notes Comput Sci Eng 43:93–107
32. Masuda S, Noguchi H (2006) Analysis of structure with material interface by meshfree method. Comput Model Eng Sci 11:131–144
33. Wu CT, Guo Y, Askari E (2013) Numerical modeling of composite solids using an immersed meshfree Galerkin method. Compos B Eng 45:1397–1413
34. Wang J, Zhou G, Hillman M, Madra A, Bazilevs Y, Du J, Su K (2021) Consistent immersed volumetric Nitsche methods for composite analysis. Comput Methods Appl Mech Eng 385:114042
35. Huang T-H, Chen J-S, Tupek MR, Beckwith FN, Koester JJ, Fang HE (2021) A variational multiscale immersed meshfree method for heterogeneous materials. Comput Mech 67:1059–1097
36. Koester JJ, Chen J-S (2019) Conforming window functions for meshfree methods. Comput Methods Appl Mech Eng 347:588–621
37. Sukumar N, Chopp DL, Moës N, Belytschko T (2001) Modeling holes and inclusions by level sets in the extended finite-element method. Comput Methods Appl Mech Eng 190:6183–6200
38. Osher S, Sethian JA (1988) Fronts propagating with curvature-dependent speed: Algorithms based on Hamilton-Jacobi formulations. J Comput Phys 79:12–49
39. Simo JC, Hughes TJR (1986) On the variational foundations of assumed strain methods. J Appl Mech 53:51–54
40. Simo JC, Rifai MS (1990) A class of mixed assumed strain methods and the method of incompatible modes. Int J Numer Methods Eng 29:1595–1638
41. Fernández-Méndez S, Huerta A (2004) Imposing essential boundary conditions in mesh-free methods. Comput Methods Appl Mech Eng 193:1257–1275
42. Dunavant DA (1985) High degree efficient symmetrical Gaussian quadrature rules for the triangle. Int J Numer Methods Eng 21:1129–1148
43. Kachanov ML, Shafiro B, Tsukrov I (2013) Handbook of elasticity solutions. Springer, Berlin

44. Fries T-P, Belytschko T (2010) The extended/generalized finite element method: An overview of the method and its applications. Int J Numer Methods Eng 84:253–304
45. Guan PC, Chi SW, Chen JS, Slawson TR, Roth MJ (2011) Semi-Lagrangian reproducing kernel particle method for fragment-impact problems. Int J Impact Eng 38:1033–1047
46. Pasetto M, Baek J, Chen J-S, Wei H, Sherburn JA, Roth MJ (2021) A Lagrangian/semi-Lagrangian coupling approach for accelerated meshfree modelling of extreme deformation problems. Comput Methods Appl Mech Eng 381:113827
47. Zienkiewicz OC, Taylor RL, Zhu J (2013) The finite element method: its basis and fundamentals. Seventh ed., Elsevier, Oxford